ABSTRACT

Title of Dissertation: DURABILITY DISTRIBUTION ANALYSIS OF LEAD-FREE SOLDER JOINTS FOR PRINTED CIRCUIT BOARD APPLICATIONS

Chien-Ming Huang, Doctor of Philosophy, 2023

Dissertation directed by: Professor Jeffrey W. Herrmann
Department of Mechanical Engineering

Fatigue models for predicting the cycles to failure of solder joints under temperature cycling situations have been discussed and developed for decades. However, most models were developed according to specific solder materials, components, and printed circuit boards in each research. There is no study to cluster and compare the fatigue models of solder joints through these different conditions. Therefore, the availability of the durability prediction of solder interconnections by using any of the available fatigue models can be unknown. On the other hand, current energy-based fatigue models for predicting the cycles to failure of the solder joint under thermo-

mechanical loadings can only provide point estimates of the characteristic life or mean life. Nevertheless, the prediction of the fatigue life should be distributions with the uncertainties. Unfortunately, no study has been found that propagates the uncertainty of the cycles to failure, especially for the solder joints under temperature cycling. Therefore, the uncertainty propagation analysis of the cycles to failure is necessary to better estimate the distribution of the fatigue life of solder joint.

The first part of this dissertation clusters and compares nine existing low-cycle energy-based fatigue models for different solder materials and components, and then analyzes major divergences between these studies. Moreover, the constants of the fatigue models are compared according to the divergences. Finite element simulation tool is applied to demonstrate the contributions of the factors on strain energy density and the variation on the predictions by applying these fatigue models. The results lead to conclusions with the advantages and limitations of using these available fatigue models for durability prediction of solder interconnections. These results provide insights that can help product designers understand and exploit the predictions of fatigue life while designing a printed circuit board and estimating its durability. In the end, precautions that can affect the prediction consistency of fatigue mode are provided for the engineers who will use these selected models or will develop their own models.

The second part of this dissertation identifies 11 uncertain input variables, which can propagate the uncertainties, via basic mechanics theory. The eigenvector dimension reduction method and FEA simulation tool are employed to determine the distribution of the system response, which is the strain energy density. Then, the distribution of strain energy density is converted to the distribution of characteristic life (in cycles) by choosing the appropriate fatigue model from the first part of this dissertation. Finally, the distribution of cumulative distribution

function of the fatigue life of solder joint is determined by taking the interval of characteristic life and specific shape parameters. In the end, this new uncertainty propagation approach can propagate the uncertainties from the material properties, geometries, and constitutive laws of the solder joint, as well as the uncertainties from strain energy density determination, low-cycle energy-based fatigue model selection, and the shape parameter from the field data in the selected fatigue life models.

DURABILITY DISTRIBUTION ANALYSIS OF LEAD-FREE SOLDER JOINTS FOR PRINTED CIRCUIT BOARD APPLICATIONS

by

Chien-Ming Huang

Dissertation submitted to the Faculty of the Graduate School of the

University of Maryland, College Park, in partial fulfillment

of the requirements for the degree of

Doctor of Philosophy

2023

Advisory Committee:

Dr. Jeffrey W. Herrmann, Chair and Advisor

Dr. Abhijit Dasgupta

Dr. Shapour Azarm

Dr. Katrina Groth

Dr. Aristos Christou, Dean's Representative

Dedication

To

My grandparents, my parents, my brothers, and my aunt and uncle

for all their support and love

Acknowledgements

First of all, I would like to express my sincere and deepest gratitude to my advisor Prof. Jeffrey W. Herrmann for his guidance and full support. Thank you for taking me as your PhD student when I decided to switch the research group in my fifth year and providing the trust and freedom to let me conduct my own research. I enjoy all the discussions with him and believe his advises on the logical thinking will lead my professional career. Thank you, Prof. Herrmann!

I would like to thank Prof. Abhijit Dasgupta, Prof. Aristos Christou, Prof. Shapour Azarm, and Prof. Katrina Groth for serving in my dissertation committee. I appreciate all their critical comments on helping the completion of this dissertation.

I would like to thank Prof. Michael Pecht for bringing me in the reliability engineering field and for guiding me to do research. I especially thank Catherine M. Hamel for providing the resources and space to enrich my teaching experience at University of Maryland, College Park. I enjoy working with her for all the semesters for Thermodynamics! I am also grateful to Hsiu-Ping Wei for guiding me through the doctoral career from the beginning. Moreover, I would like to thank Jack Yang, Shao-Peng Chen, and Cheng-Yi Lee for their support and encouragement.

In the end, I would not have all my accomplishments without the full support from my family, especially from my mother and younger brother. They always believe me and never stop me from looking for what I really have passion for. Without their sacrifice, I would not be in the United States as well as earn my doctoral degree.

Table of Contents

List of Tables

List of Figures

List of Abbreviations

BGA	–	Ball Grid Array
CDF	–	Cumulative Distribution Function
CTE	–	Coefficient of Thermal Expansion
CTF	–	Cycles to Failure
EDR	–	Eigenvector Dimension Reduction
FEA	–	Finite Element Analysis
GA	–	Garofalo-Arrhenius
I/O	–	Input/Output
LCR	–	Leadless Chip Resistor
MCS	–	Monte Carlo Simulation
PBGA	–	Plastic Ball Grid Array
PCB	–	Printed Circuit Board
PDF	–	Probability Density Function
QFN	–	Quad Flat No-lead
RoHS	–	Restriction of Hazardous Substances
RSM	–	Response Surface Method
SAC	–	Sn-Ag-Cu
WLCSP	–	Wafer Level Chip Scale Package

Chapter 1: Introduction

This chapter is organized as follows. In Section 1.1, the motivation and objectives of this dissertation are described. Section 1.2 points out the organization of the dissertation.

1.1 Motivation and Objectives

To comply with European RoHS legislation, lead-free solder materials have been widely used in the electronic products since 2006 [1]. Due to the concerns with cost reduction and field applications, newly-developed lead-free solders have been being introduced. Moreover, the rapid growth of electronics industry also pushes the introduction speed of new solder materials and electronic components [2]. Therefore, evaluating the durability of the solder joints for the new products can be challenging for engineers who are designing electronic systems.

The number of electronic components keeps increasing in a single product or system because of the technology development, including autonomous driving and data center. Therefore, the reliability of a single electronic component is critical for the system reliability. Among the major failure mechanisms of the electronic components, the fatigue of solder joints induced by recurring temperature changes is considered as major contributor [3]. Predicting the fatigue life of solder joints under the thermo-mechanical loadings becomes necessary while designing the new products.

The cost of both time and resources for new product qualification is expensive, so the engineers would like to be confident on the pass rate before proceeding the qualification step. Finite element analysis (FEA) simulation is an efficient tool to estimate the performance of the product under specific loadings during the product design phase, so it can provide insights for the

engineers to improve the products and prevent unnecessary loss for the product qualification. Notwithstanding the advantages of FEA simulation, the curse of dimensionality and the uncertainty propagation need to be handled before running the simulation. While the number of input variables increases, the computational costs surge exponentially. Moreover, each input variable has uncertainty, and the uncertainty can be propagated to the final outcomes. Therefore, the inputs and outputs of the FEA simulation should be carefully reviewed and handled. The inputs include the material properties and geometries of the product, and the loading conditions. The outputs can be any type of the damage metric. Without processing the inputs and outputs appropriately, the FEA simulation will not provide its true values.

A fatigue life model for solder joints is useful for optimizing the product design and the assembly process, including material and component selection, and predicting the durability in the field according to the loading conditions. Moreover, the development time and costs can be reduced because the modeling and simulation procedures can provide approximate results with much lower time and resources than testing.

Many studies working on the reliability of solder joints under temperature cycling have been published for decades. However, all the studies conducted their own experiments and FEA simulations to obtain the information of cycles to failure (CTF) and damage metrics and then used curve fitting techniques to get the coefficients and exponents of specific equation. This equation was then employed to plot the relationship between the CTF and damage metric, and compared to the data points from the experiments and simulations. The R-squared (R^2) was always great between the proposed equation and the data points. After that, the authors recommended their equation for the CTF prediction of the solder joints. Nevertheless, there were several of this kind

of single research to report their equations for predictions [4]−[11]. The equations can be different due to the type of fatigue model, and the CTF predictions of the equations can be divergent for many reasons. The engineers need to have a better idea which equation is appropriate for their product and what the limitations are while using the equation.

As defined by Matt et al. [12], meta-analysis fosters empirical knowledge about causal associations by combining findings from many different but related studies. The generated knowledge provides more trustworthy points than any single study does. Therefore, meta-analysis is an appropriate technique to analyze the published CTF prediction studies and is necessary to translate their research results to practical usage [13]. Unfortunately, meta-analysis has not been applied for electronics reliability research. This dissertation will employ a type of meta-analysis in fatigue model and material constitutive equation screening.

The uncertainties of the prediction from a fatigue model come from different places, including the material constitutive equations, manufacturing-related variables (material properties and dimensions), and the constants of the fatigue models. Uncertainty propagation analysis can incorporate these uncertainties to determine the statistical distributions of the system responses, such as time to failure, through computational models. However, the electronic components involve sophisticated geometries and non-isotropic or nonlinear material properties. These facts induce a large number of input variables. Thus, traditional uncertainty propagation techniques are not appropriate for application due to the concerns with computational costs [14].

There are two objectives in this dissertation. The first objective is to demonstrate the prediction differences among the available low-cycle energy-based thermo-mechanical fatigue models for solder joint. The second objective is to develop an uncertainty propagation approach to

propagate the uncertainties while determining the distribution of cumulative distribution function for a solder joint.

1.2 Organization of the Dissertation

Chapter 1 describes the motivations and two objectives of this dissertation. Chapter 2 reviews the literatures about the evolution of lead-free solders, life cycle trend of electronic materials and parts, CTF prediction of solder joints under temperature cycling, Garofalo-Arrhenius (GA) creep constants, Anand parameters, eigenvector dimension reduction (EDR) method, and meta-analysis. Chapter 3 describes research questions and approaches, including the meta-analysis flow, simulation methods, and application of EDR method.

Chapter 4 presents durability distribution analysis of lead-free solder interconnections for printed circuit board applications by comparing low-cycle energy-based thermo-mechanical fatigue models. First, we clustered and reviewed nine existing energy-based fatigue models and then pointed out the key differences between these models. We then conducted FEA simulations in ANSYS Workbench environment with same temperature cycling profile. The results of accumulated strain energy density are compared with different conditions, including volume-weighted averaging amounts, energy types, and cycles for determining strain energy density. Moreover, we developed adjustment methods for the predictions of fatigue models and verified these with finite element analysis (FEA) simulations. The distribution of the predictions on cycles to failure among the fatigue models is significantly reduced after applying the adjustments, and exhibited excellent consistency around 1 mJ/mm^3 strain energy density. This chapter was submitted to The 24th European Microelectronics & Packaging Conference.

Chapter 5 discusses durability distribution prediction of thermo-mechanical solder fatigue failure with both simulation and manufacturing input variables by eigenvector dimension reduction (EDR) method. The uncertainties of the uncertain input variables are first classified. The EDR method is then introduced and implemented to the uncertain input variables to get the probability density function (PDF) of each input variables. Construction of the PDF of system response is performed after calculating its first four statistical moments. The cumulative distribution function (CDF) of the characteristic life (N63.2%) was then obtained via the selected low-cycle energy-based fatigue models and eventually the distribution of the CDF of the solder joint was provided. This chapter was submitted to *IEEE Access*.

Chapter 6 first provides short summary and conclusions of this dissertation. Major contributions are then addressed. In the end, external validity of this dissertation is discussed and outlined as the future work to fit in larger scheme.

Chapter 2: Literature Reviews

This chapter is organized as follows. In Section 2.1, fatigue models are reviewed and the key parameters of the fatigue models are summarized. Section 2.2 compares the temperature cycling profiles from the fatigue models mentioned in Section 2.1 and compares them to the JEDEC standard. Section 2.3 addresses the state of art of the constitutive laws for the solder joint. Section 2.4 reviews the volume-weighted averaging technique while dealing with the FEA simulation results. The popular uncertainty propagation methods are reviewed in Section 2.5. In Section 2.6, we describe the research gaps.

2.1 Fatigue Models

During temperature cycling, solder fatigue is the major failure mechanism [15]. The solder fatigue comes from the coefficient of thermal expansion (CTE) mismatch between the component and the PCB, and the fatigue has been a known issue in the electronics industry since late 1950s [16]. Creep behaviors dominate the failure mechanism for solder joints experiencing elevated temperatures, and a combined creep and fatigue mechanism can also happen while the elevated temperature and temperature cycling loading happen simultaneously, and this can be called as creep-fatigue failure mechanism [17]. This is considered as one of the major failure mechanisms of the solder joint in electronic products [3].

Consequently, numerous models that describe the impact of thermal cycling on solder interconnections have been developed and studied. These solder fatigue models can be formulated with cyclic strain, cyclic strain energy density, or cyclic stress. Lee *et al.* [18] and Su *et al.* [19] reviewed the models that predict the fatigue failures of solder interconnections and categorized

them into plastic strain-based fatigue models, creep damage-based fatigue models, energy-based fatigue models, and damage accumulation-based fatigue models. In general, temperature cycling induced fatigue failure for the solder interconnections belongs to low-cycle fatigue (< 10,000 cycles). Most studies working on the fatigue models of solder interconnection under temperature cycling applications were related to inelastic strain-based fatigue models and energy-based fatigue models.

Among the four types of fatigue models, energy-based fatigue models have been frequently used in recent years. For the fatigue models with cyclic strain energy density formulation, both viscoplastic [20] and creep-only [21] energy models have been proposed. (Viscoplastic models include both creep energy and plastic energy.) In general, the energy-based fatigue model is based on the hysteresis loop of the material, which is a volume-weighted stress-strain relationship. The energy density accumulation can be calculated by correlating the energy under the stress-strain hysteresis loop. Dasgupta *et al.* [21] noted that strain energy density incorporated both the information of stress and strain, so it was a good indicator for solder fatigue failure.

Morrow's solder fatigue model [20] has been used to predict the cycles to failure of the solder joint. Solomon and Tolksdorf [22], and Shi et al. [23] modified Morrow's model to improve its accuracy. Akay et al. [17] combined Engelmaier model and energy-partitioning approach to propose a solder fatigue life model involving creep-fatigue behaviors. Syed [24] considered the cyclic loading as a special case of creep, and proposed a prediction model based on Monkman–Grant equation [25] and Miner's rule [26]. Syed [5] then suggested two fatigue life prediction models for Sn-Pb and Sn-Ag-Cu solders based on creep strain and creep strain energy density. The assumption Syed made was considering the damage of the solder joint during the temperature

cycling was contributed by the steady-state creep strain accumulation. Due to popularity of the fatigue studies by Syed [5] and the simplicity of the fatigue model, many studies have referred to this type of fatigue model, and several sets of constants for the fatigue model have been published [4]–[11].

In general, a damage model with an inverse power law form connects the relationship between the damage metric and cycles to failure. Damage metrics include accumulated inelastic strain range and strain energy density, and the cycles to failure can be mean life (50% failures) or characteristic life (63.2% failures in Weibull distribution). Let N_f be the cycles to failure. Let D be the damage metric, and let A and n be the material constants, which can be affected by many factors, including solder materials, temperature cycling profile, and assembly structure. Then, Equation (2.1) is a generalized fatigue life model for solder joint under temperature cycling [4].

$$N_f = (A \times D)^n \tag{2.1}$$

The cycles to failure of a solder joint can be estimated by applying the power law to fatigue coefficient, fatigue exponent, and damage metric, as addressed in Equation (2.1). Many solder fatigue life constants have been proposed for Sn-Ag-Cu (SAC) solder joint under various temperature cycling conditions. Table 1 lists the fatigue coefficients and exponents for solder joint fatigue life models from prior studies that determined these values by fitting the power law fatigue model to experimental data and simulation results. For the fatigue life prediction, N50% means the cycles that 50% of the solder joints fail, and N63.2% means the cycles that 63.2% of the solder joints fail. As shown in Table 1, the damage metric in the fatigue model was categorized into two

groups, which were viscoplastic strain energy density and creep strain energy density. This dissertation will discuss the prediction difference between these two groups in Chapter 4. On the other hand, the employed solder materials and the dimensions of the solder joints, component, and PCB were summarized in Table 2 for subsequent comparison purpose.

Table 1 Energy-based low-cycle fatigue solder fatigue life models

Prior studies	Strain energy density	Fatigue coefficient	Fatigue exponent	Fatigue life prediction
Chen et al. [4]	Viscoplastic	1.05×10^{-5}	-0.59	N50%
	Creep	4.75×10^{-6}	-0.55	N50%
Syed [5]	Creep	1.90×10^{-3}	-1.00	N50%
Schubert et al. [6]	Viscoplastic	3.30×10^{-3}	-1.02	N63.2%
Hsieh [7]	Creep	4.15×10^{-6}	-0.60	N50%
Hsieh and Tzeng [8]	Creep	1.09×10^{-2}	-2.26	N63.2%
Ghorbani and Spelt [9]	Creep	2.70×10^{-2}	-2.27	N50%
Sun et al. [10]	Creep	4.38×10^{-8}	-0.39	N63.2%
Zhang et al. [11]	Viscoplastic	1.69×10^{-4}	-0.77	N63.2%

Table 2 Key summary for the selected fatigue models

Literature	Solder materials	Dimensions of solder joint, component, and PCB
Chen et al. [4]	Mixed soldering Solder ball: SN100C, SAC0307, SAC105, SAC107, SAC205, SAC305, SAC405 Solder paste: SN100C, SAC305	192 I/O BGA Component: 14 mm by 14 mm Solder ball: 0.48 mm diameter and 0.3 mm height 84 I/O BGAs Component: 7 mm by 7 mm Solder ball: 0.3 mm diameter and 0.2 mm height
Syed [5]	Solder ball: SAC405 and SAC395 Solder paste: Sn-Ag-Cu	208 I/O BGAs Component: 15 mm by 15 mm Solder ball: 0.46 mm diameter and 0.3 mm height 64 I/O BGAs Component: 8 mm by 8 mm Ball: 0.46 mm diameter and 0.3 mm height
Schubert et al. [6]	SAC387	PBGAs 256 I/Os and 272 I/Os Die: 10 × 10 mm Substrate thickness: 0.56 mm PCB thickness: 1.57 mm
Hsieh [7]	SAC405	WLCSPs I/Os: 100, 144, 151 Die size: 4 × 4 mm and 6 × 6 mm Ball diameter: 0.18, 0.20, 0.25 mm Ball height: 0.108, 0.125, 0.163 mm
Hsieh and Tzeng [8]	SAC105	WLCSPs I/Os: 121 Die size: 5.3 × 5.3 mm Ball diameter: 0.25 mm Ball height: 0.19 mm
Ghorbani and Spelt [9]	SAC387	Leadless chip resistors (LCRs) Component: 6.30 x 3.20 mm; 0.65 mm height Solder joint: 0.76 x 3.20 mm; 0.12 mm height PCB thickness: 1.23 mm
Sun et al. [10]	SAC405	QFNs I/Os: 32, 40, 56 Component: 5 x 5 x 0.9 mm; 8 x 8 x 0.9 mm Solder joint: 75 μm stand-off height

		PCB thickness: 2.35 mm
Zhang et al. [11]	SAC387	PBGA352: ball (0.76 mm, pitch 1.27 mm); component (35 x 35 x 2.29); die (12.3 x 12.3 x 0.30) fleXBGA144: ball (0.46 mm, pitch 0.80 mm); component (12 x 12 x 1.09); die (8.95 x 8.95 x 0.27) TABGA96: ball (0.30 mm, pitch 0.50 mm); component (8 x 8 x 0.97); die (5.14 x 5.14 x 0.31) BT48A: ball (0.30 mm, pitch 0.75 mm); component (8.23 x 5 x 0.76); die (7.49 x 4.45 x 0.27) TV46: ball (0.30 mm, pitch 0.75 mm); component (7.87 x 5.76 x 0.83); die (7.47 x 5.51 x 0.43) PCB thickness: 1.6 mm

2.2 Temperature Cycling

For the temperature cycling profile, we referred to JEDEC JESD22-A104F standard Condition G [27], which had the following values: Minimum temperature (−40˚C), maximum temperature (125˚C), ramp rate (8˚C/minute for both heating and cooling), dwell time (10 minutes for both maximum and minimum temperatures), and the process time was almost one cycle per hour (2.78×10^{-4} Hz). A general temperature cycling profile with critical parameters was shown in Figure 1. After summarizing the temperature cycling profile from the available solder joint fatigue studies with strain energy density model, these studies basically obeyed the criteria in JESD22-A104F. This fact also helped the comparison between these models.

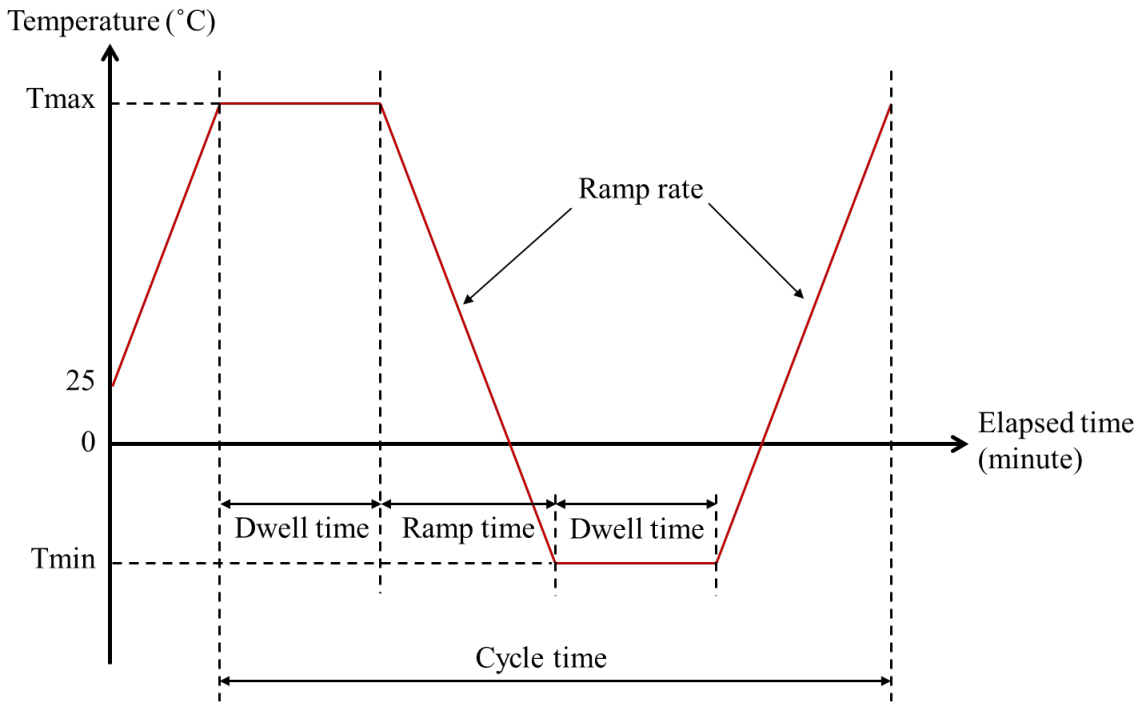

Figure 1 General temperature cycling profile

Although the fatigue life is affected by the temperature cycling frequency [23], most of the studies listed in Table 3 applied a frequency within 1.39×10^{-4} Hz and 2.78×10^{-4} Hz, which is a relatively narrow window of the cycling frequency. Hence, the effect of cycling frequency on the fitting of fatigue model constants can be ignored while comparing the fatigue models in this study.

Table 3 Temperature cycling profiles from the selected studies

Literature	Min. Temperature (˚C)	Max. Temperature (˚C)	Ramp rate (˚C/min.)	Dwell time (min.)	Cycles per hour
Syed [5]	−40	125	11	15	1
	−55	125	15	3	2
	0	100	10	5	2
Chen et al. [4]	−40	125	8	10	0.98
Schubert et al. [6]	−55	20	14	10	2
	0	70			
	50	120			
Schubert et al. [6]	−55	125	36	10	2
	−55	150	41		
Schubert et al. [6]	−40	125	11 [28]	15 [28]	1 [28]
	−40	150	--	--	1.36
Hsieh [7]	−40	125	11	10	1.24
			16.5	15	
Hsieh and Tzeng [8]	−40	125	9.9	15	0.95
Ghorbani and Spelt [9]	0	100	14	5	2.47
	0	100	95	5	4.96
	−40	125	95	5	4.45
Sun et al. [10]	−40	125	11	15	1
Zhang et al. [11]	−55	125	Ramp up: 6 Ramp down: 10	15 at 125 ˚C 10 at −55 ˚C	0.8
This dissertation	−40	125	8	10	0.98

2.3 Constitutive Relationships

The plastic and creep deformation of the solder joint make contributions to the strain energy density accumulated among temperature cycles. During the FEA simulation, the strain energy density can be modeled as lump sum (entire inelastic part) or energy partitioning (elastic + plastic + creep). When the solder joint is subjected to the temperature cycling, the homogeneous

temperature, T_h, of the solder joint is above 0.4 for the entire process. T_h is defined as the ratio of the ongoing process temperature, T(t), to the melting temperature of the material, T_m. Thus, $T_h = T(t)/T_m$. The unit of both T(t) and T_m are in Kelvin scale. Material degradation behavior, such as creep, happens when Th is greater than 0.4 [29]. Therefore, the creep behavior of the solder joint should be a critical concern under the temperature cycling conditions. Figure 2 shows an idealized creep-rupture curve of metals or alloys [30]. As shown in Figure 2, the total strain to rupture consists of elastic, plastic, and creep strain, and the creep strain is dominant in the strains.

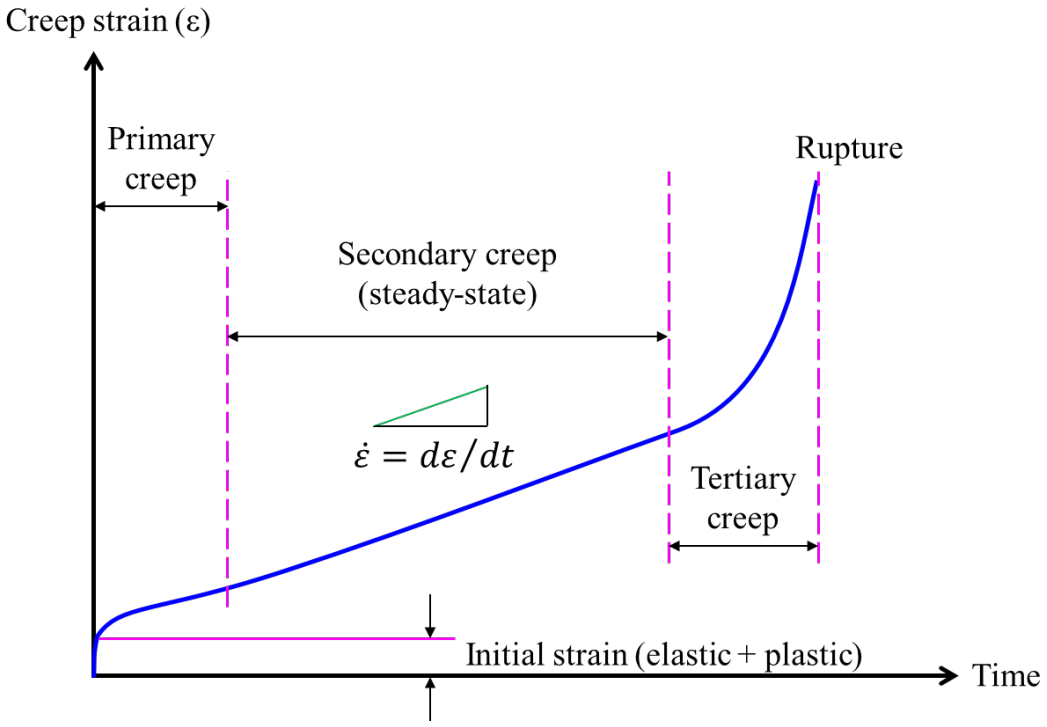

Figure 2 Idealized creep-rupture curve of metals or alloys (adapted from Garofalo's book in 1965)

Many studies have worked on the fatigue life prediction of solder joints with strain energy density. Some models focused on viscoplastic strain energy density, whereas other models focused creep only strain energy density. While fitting the constants of fatigue model, utilizing different type of strain energy density would generate different numbers of the constants. Moreover, employing an established fatigue model without understanding its underlying assumptions can make significant deviation on the prediction of fatigue life. For example, applying the creep only strain energy density into a lump sum fatigue model can produce an under-estimated fatigue life.

For viscoplastic strain energy density research, the Anand viscoplastic constitutive model [31] has been widely used in the analysis of mechanical behavior of lead-free solder materials and electronic packaging field. The Anand model incorporates the creep strain and plastic strain as a unified inelastic strain. The Anand parameters model contains three equations, including one flow equation and two evolution equations [31], as shown in Equation (2.2) to (2.4).

Equation (2.2) is the constitutive equation for the plastic strain rate, as known as the flow equation, where $\dot{\varepsilon}_p$ is the plastic strain rate, T is the absolute temperature, Q is the activation energy, A is the pre-exponential factor, ξ is the multiplier of stress, and m is the temperature-dependent strain rate sensitivity.

$$\dot{\varepsilon}_p = Ae^{-\left(\frac{Q}{RT}\right)}\left[\sinh\left(\xi\frac{\sigma}{s}\right)\right]^{\frac{1}{m}} \tag{2.2}$$

Equation (2.3) and Equation (2.4) are the equations of the evolution of the internal variable s and its saturation value s^*, respectively. $h(\sigma, s, T)$ is the strain hardening rate, h_0 is the hardening

constant, a is the strain rate sensitivity of the hardening process, and s^* is the saturation value of the deformation resistance. n is the strain rate sensitivity of the saturation value of the internal variable s.

$$\dot{s} = h(\sigma, s, T)\dot{\varepsilon}_p$$
$$\dot{s} = h_0 \left(1 - \frac{s}{s^*}\right)^a \dot{\varepsilon}_p \; ; \; \text{a} > 1 \tag{2.3}$$

$$s^* = \hat{s} \left[\frac{\dot{\varepsilon}_p}{A} e^{\left[\frac{Q}{RT}\right]}\right]^n \tag{2.4}$$

After integrating Equation (2.3), the equation of s can be expressed in Equation (2.5), where s_0 is the initial value of the internal variable s.

$$s = s^* - \left[(s^* - s_0)^{(1-a)} + (a-1)\{h_0 (s^*)^{-a}\}\varepsilon_p\right]^{\frac{1}{1-a}} \tag{2.5}$$

The nine material parameters of Anand parameters model can be determined from the stress-strain curve of the material and curve fitting technique. Moreover, the nine-parameter format of Anand viscoplastic constitutive model has been built in the popular commercial FEA software, including ANSYS, for users to fill in their specific numbers for simulation. Nevertheless, the strain energy density from FEA simulation is related to the values of Anand parameters, and the reported values from the literatures exhibits a wide range for lead-free solders. For instance, the Anand

parameters for SAC305 solder have been reported in recent years [32]−[41], and are summarized in Table 4.

Table 4 Summary of Anand parameters for SAC305 solder material

Code Name	Anand Parameters								
	s_0 (MPa)	Q/R (K)	A (s^{-1})	ξ	m	h_0 (MPa)	$\hat{s}$ (MPa)	n	a
Tensile[1] [32]	21.0	9,320	3,501	4	0.250	180,000	30.2	0.01	1.78
Tensile[1] [33]	5.50	11,900	4,000	4.00	0.47	30,000	5.00	0.059	1.60
Tensile [34]	1.0665	10,413.3	142,830,000	1.472	0.141446	5,023.9	20.2976	0.032472	1.120371
Tensile [35]	2.45	6,067.6	717.260	2	0.130	14,560	29.0	0.0436	2.22
Creep[1] [36]	5.1	3,468	0.000931	3.2	0.065	49,000	16.4	0.078	4
Creep[1] [37]	16.33	9,096	3,518	4	0.188	160,000	24.64	0.015	1.79
Creep [38]	6.0001	7,435.3	3,564.7	3.1479	0.24387	20,051	29.652	0.015665	2.1314
Shear [34]	1.0665	10,413.3	82,465,000	2.550	0.141446	5,023.9	20.2976	0.032472	1.120371
Shear [39]	2.15	9,970	17.994	0.35	0.153	1,525.98	2.536	0.028	1.69
Unknown[2] [40],[41]	45.9	7,460	5,870,000	2.00	0.0942	9,350	58.3	0.015	1.50

- Superscript 1 means the four studies were from the same research group.
- Superscript 2 means the original literature (MS thesis) couldn't be found. The journal paper, which cited the original literature, was also referred in this paper.

Viscoplastic strain energy density is composed of plastic and creep strain energy densities. In this dissertation, the multilinear isotropic hardening model was utilized to handle the plastic strain energy density and the Garofalo-Arrhenius creep model [30] was applied to estimate the creep strain energy density. The Garofalo-Arrhenius creep model is composed of a hyperbolic sine equation with stress-dependent term and an Arrhenius equation with temperature-dependent term, as shown in Equation (2.6), where C_1 and C_2 are coefficients related to the material, σ is applied stress, C_3 is stress exponent, C_4 is activation energy divided by Boltzmann's constant, and T is temperature in Kelvin scale. Many studies have been published to establish data sets of Garofalo-Arrhenius parameters for lead-free solder materials [42]−[48]. Table 5 summarized the Garofalo-Arrhenius parameters employed in this dissertation. For the convenience of discussion in this dissertation, a code name was used instead of the original name for each study.

$$\frac{d\varepsilon_{cr}}{dt} = C_1 \times [\sinh(C_2 \times \sigma)]^{C_3} \times exp\left(-\frac{C_4}{T}\right) \tag{2.6}$$

Table 5 Summary of Garofalo-Arrhenius creep constants for solder material

Solder alloy	Code name	Garofalo-Arrhenius Parameters			
		C_1 (s^{-1})	C_2 (MPa^{-1})	C_3	C_4 (K)
SAC305 [4]	GA01	6.07	0.18	2.3	6,710
SAC387 [6]	GA02	277,984	0.02447	6.41	6,500
SAC405 [7]	GA03	1.15×10^6	0.0335	7.5	8,703.4
SAC105 [8]	GA04	2.31×10^6	0.026	6.5	6,962.7
SAC387 [9]	GA05	441,000	0.005	4.2	5,412
SAC387 [11]	GA06	1.5×10^3	0.19	4	8,575.9

The multilinear isotropic hardening property was utilized to model the time-independent plastic strain (ε_{pl}). The relationship between the applied stress and strain was addressed in Equation (2.7) to (2.9) [4], where σ is the instantaneous stress, K and n_{pl} are temperature-dependent instantaneous plasticity material constants, and T is temperature in Celsius scale. Moreover, the multilinear isotropic hardening curves were taken from ANSYS Workbench and shown in Figure 3.

$$\varepsilon_{pl} = \left(\frac{\sigma}{K}\right)^{\left(\frac{1}{n_{pl}}\right)} \tag{2.7}$$

$$K = 121.6 - 0.4T \tag{2.8}$$

$$n_{pl} = 0.29 - 0.00046T \tag{2.9}$$

Because the contribution of creep strain energy density is much higher than plastic one (around 10 times higher), this dissertation only employed one prior study for the multilinear isotropic hardening property, as addressed in Equation (2.7) to (2.9), to simplify the comparison process.

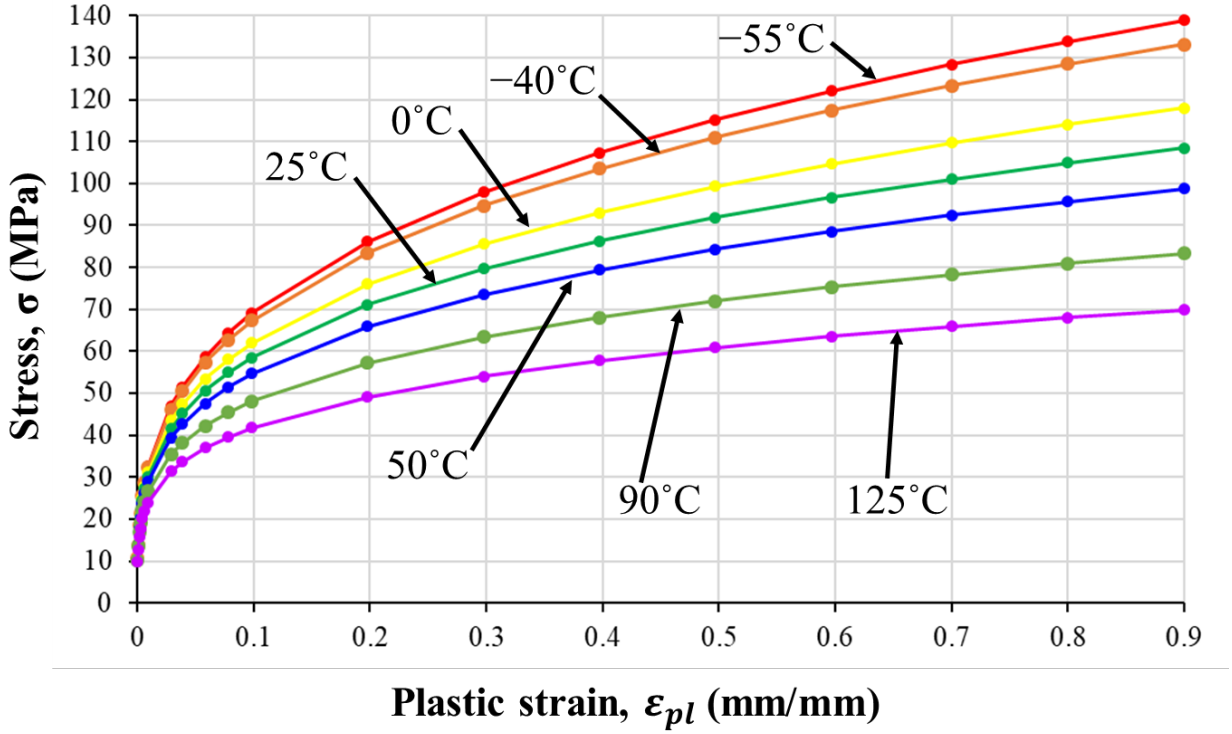

Figure 3 Multilinear isotropic hardening curves

2.4 FEA: Volume-Weighted Averaging Technique

In early research on fatigue life, the strain accumulation was employed as the damage metric to calculate the fatigue life of leadless components with a good prediction. However, singularity

issues happened while increasing the mesh density of the FEA model [49]. The maximum stress and strain existed in the discontinuities of materials and geometries. In order to catch these maximum values, using finer meshes was necessary for the modeling. However, increasing the mesh density was computationally expensive and no clear guidance was defined for the mesh density. These concerns put difficulties on predicting the fatigue of solder joints. Therefore, a methodology, as known as volume-weighted averaging technique, was developed by Bilgic [50] to predict the fatigue life without relying on the increasing of mesh density. The concept of volume-weighted averaging technique assumes that the failure of the solder joint was caused by the entire solder joint instead of a single element. Each element of the solder joint meshes made proportional contribution to the failure of solder joint according to the corresponding volume [17]. Therefore, the volume-weighted averaging stress and strain can be written as the following Equation (2.10) and (2.11), where σ_{ij}^{e} and ε_{ij}^{e} were the stress and strain components in each element e, respectively. V^{e} was the volume of the element e. By applying this technique, the effect of the increased stress and strain value due to the increasing mesh density was compensated by the decreased element size itself. Furthermore, Akay et al. [17] and Bilgic [50] reported the stress and strain value determined from the volume-weighted averaging technique were not sensitive to the effects of mesh density. In this dissertation, the strain energy density accumulation was also calculated by the volume-weighted averaging technique, and we used Equation (2.12) to do so.

$$\sigma_{ij_{ave}} = \frac{\sum \sigma_{ij}^{e} \cdot V^{e}}{\sum V^{e}} \tag{2.10}$$

$$\varepsilon_{ij_{ave}} = \frac{\sum \varepsilon_{ij}^{e} \cdot V^{e}}{\sum V^{e}} \tag{2.11}$$

$$W_{ij}{}_{ave} = \frac{\sum_{i=1}^{n} V_i \times W_i}{\sum_{i=1}^{n} V_i} \tag{2.12}$$

2.5 Uncertainty Propagation

The prediction of the fatigue model only provides a point estimate, such as mean life (N50%) or characteristic life (N63.2%). The uncertainty of the fatigue life needs to be addressed to understand the uncertainty of the predictions. In short, the PDF of the prediction of fatigue life needs to be provided, so the uncertainty propagation analysis is necessary.

The uncertainty propagation analysis is able to characterize the output distribution of a system with incorporating the input uncertainties. The most popular uncertainty propagation methods are response surface method (RSM) and random sampling method. For response surface method, there is a limitation on the number of uncertain input variables, so it is not practical to use this method to deal with complicated system with a lot of input variables. On the other hand, the computational efforts of the random sampling method, such as Monte Carlo simulation (MCS), is independent of the number of uncertain input variables. However, statistical variations exist for the system output, including failure probability, by utilizing the random sampling method. To ensure the accuracy of

the system output, large number of simulations is required. Figure 4 addresses the required number of modeling runs with various uncertainty propagation methods according to the number of input variables.

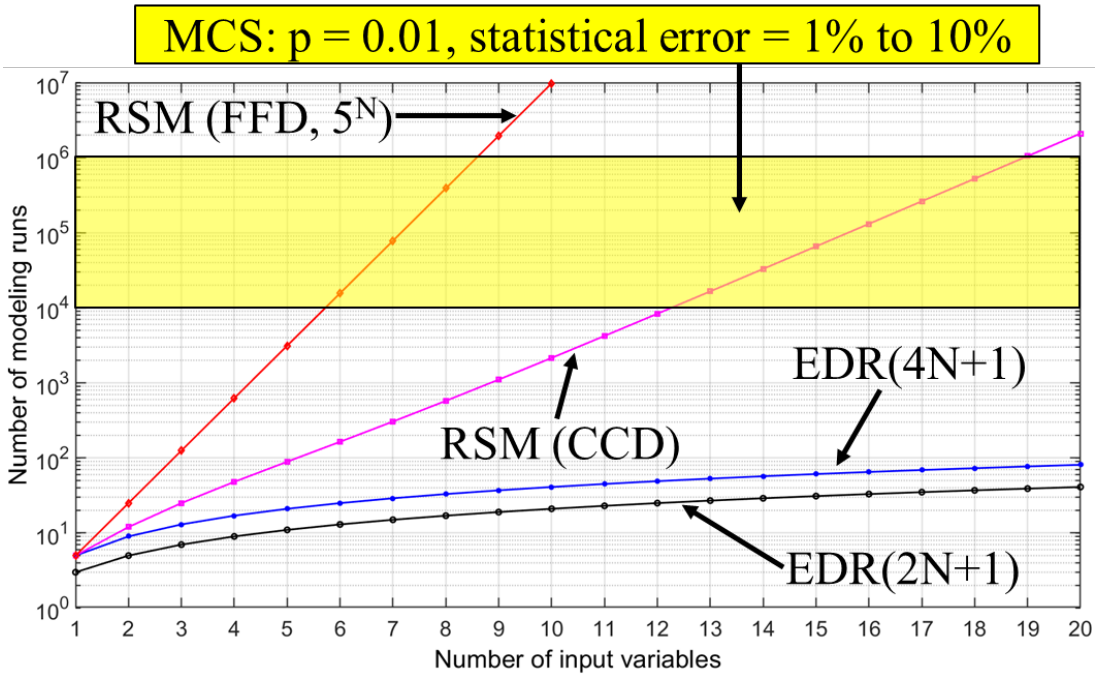

Figure 4 The number of modeling runs with various uncertainty propagation methods

Eigenvector dimension reduction (EDR) method [72] was developed to deal with the extremely large computational efforts, especially in the reliability field, which exists many nonlinear computational models, such as viscoplastic strain energy density calculation. For instance, EDR method has been applied for determination of the warpage of fan-out wafer level package (FO-WLP) [51] and the material properties of solder joint in leadless chip resistors (LCRs) [52].

2.6 Research Gaps

After reviewing the literatures, we found that there is no systematic study on the low-cycle energy-based fatigue model studies by incorporating the common solder materials and components. Moreover, the published uncertainty propagation studies only qualified the uncertainty of specific physical quantities or material properties. We haven't found any study working on the uncertainty qualification of the fatigue life of the solder joint.

Chapter 3: Research Questions and Approaches

This chapter is organized as follows. In Section 3.1, the problem statements are described. Section 3.2 lists the research questions, and Section 3.3 introduces the research approaches.

3.1 Problem Statements

Although previous research has proposed the low-cycle energy-based fatigue model for specific components under temperature cycling, engineers do not have an idea on which model they can utilize for their own components if the components are different from the ones in the previous research. Moreover, the published low-cycle energy-based fatigue models can only predict point estimate of the mean life or characteristic life of the solder joint. The engineers still do not know the distribution of that point estimate as well as the cumulative distribution function of the cycles to failure.

3.2 Research Questions

In order to address these problems and add to our knowledge of predicting the solder joint reliability under temperature cycling conditions, this dissertation will address the following research questions:

1. What are the major differences between the published low-cycle energy-based fatigue models for the solder joints under temperature cycling?
2. Can these fatigue models be used to predict the cycles to failure for different solder materials and components?

3. What are the uncertainties for determining the strain energy density of the solder joint under thermo-mechanical loadings and what are their contributions?
4. What is the most efficient way to perform the uncertainty propagation for the solder joints under temperature cycling?

3.3 Research Approaches

In this dissertation, we used a BGA component on the PCB as an example to demonstrate the fatigue life prediction on the solder joints under temperature cycling condition. Figure 5 is a basic flow of predicting the CTF of the solder joint by using the FEA simulation tool, where ΔW is the strain energy density accumulation, and N_f is the number of cycles to failure. To support the reproducibility of this work, the design files are obtained from open sources. The detail information is addressed in Chapter 4. For the main stream of this flow, which does not consider the uncertainty propagation, the FEA model is generated according to the information from the design files via ANSYS tools.

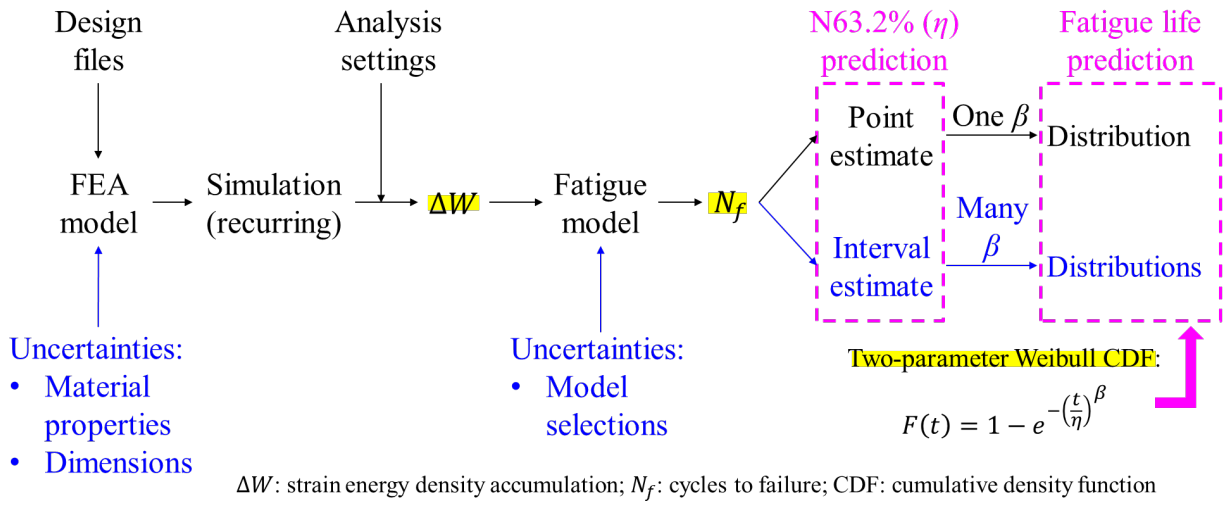

Figure 5 CTF prediction flow via FEA simulation

The first two research questions are answered in Chapter 4. The strain energy density accumulation is the outcome of the simulation in this dissertation, and it is also the input of the fatigue model to predict the CTF. The selection and comparison of the fatigue models in this dissertation follows the procedure of the meta-analysis, as shown in Figure 6. Therefore, the major differences between these low-cycle energy-based fatigue models can be compared to answer the first research question. After the differences of the fatigue models are identified, the prediction of the CTF can be normalized among the models. The normalized predictions support the answers of the second research question.

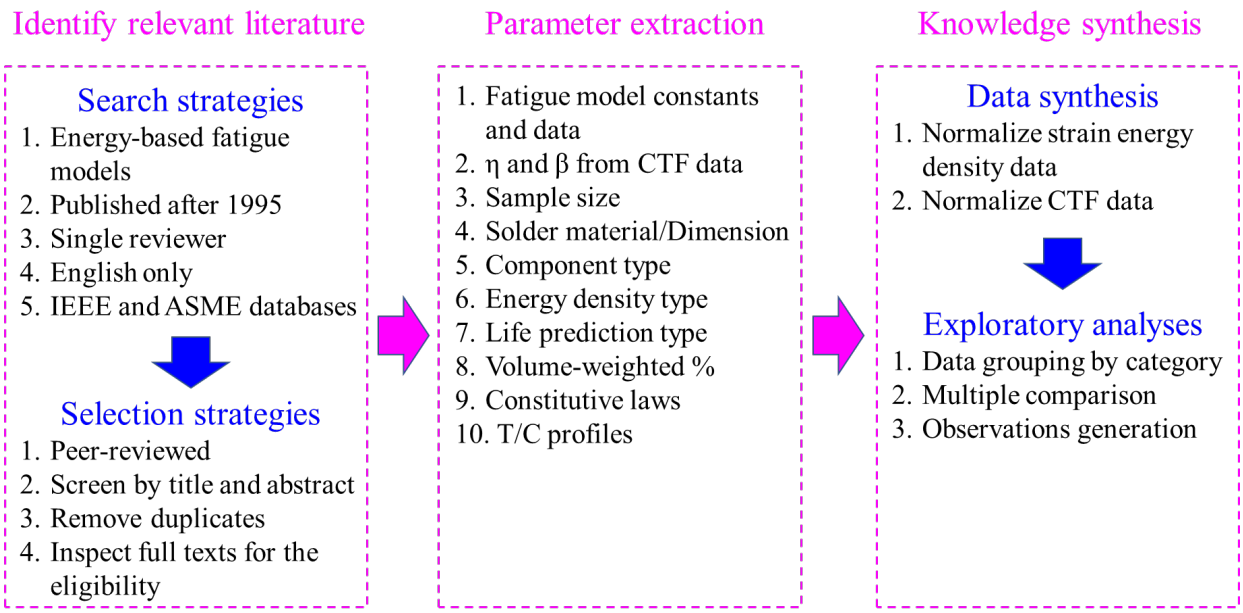

Figure 6 Meta-analysis procedure

The third and fourth research questions are answered in Chapter 5. The input variables with the uncertainties from the FEA simulation are first identified and then the uncertainty propagation during the simulation is handled with the EDR method and Pearson system. The results answer the third research question. In the end, the distributions of the fatigue life are determined by applying the interval values of scale parameter and shape parameter for the cumulative distribution function of the Weibull distribution, and answer the fourth research question.

Chapter 4: Energy-Based Fatigue Models Comparison

This chapter is organized as follows. In Section 4.1, the need of comparing the available low-cycle energy-based fatigue models are described. Section 4.2 presents the analysis approach with ANSYS simulation tools. Section 4.3 and 4.4 present and discuss the simulation results and the adjustment of predictions on cycles to failure. Section 4.5 concludes this chapter.

4.1 Introduction

The increasing functionality and complexity of electronic products has led to smaller chips and higher interconnection density [53],[54]. The reliability of the solder interconnection is critical in modern electronic products because the solder joints provide mechanical and electrical connections between chips, components, and printed circuit boards (PCBs). The solder interconnection can fail due to various loading conditions, including temperature cycling, vibration, or drop/shock impact [55],[56]. Among these loading conditions, temperature cycling induced low-cycle fatigue is considered as a one of the major failure mechanisms for the electronics.

The reliability depends, in part, upon the choice of solder. As manufacturers have sought ways to reduce the environmental impact of their product and to comply with regulations about hazardous materials and the disposal of electronic products, lead-free solders have become the major solder materials used in the electronic products, especially in consumer products. Many lead-free solders have been developed during the past 20 years because of various considerations, including cost and reliability, and the component-level and board-level reliability performance of different lead-free solders has been reported in the literature [57]−[64]. These results, which

provide some insights about the performance of different solders, are based on experiments and finite element analysis (FEA) simulations with specific lead-free solders and assemblies.

An engineer who is developing a new product and wishes to use a specific solder material should conduct reliability tests with prototypes of the new system. Performing the entire series of reliability tests can be time-consuming and costly, however. Therefore, FEA simulation tools, such as ANSYS, have become a popular technique to analyze the reliability of solder interconnections in the electronics industry [65]−[68] in order to have a preliminary idea of the reliability of developing product without running costly reliability tests. The results from such simulations depend upon multiple parameter values and modeling choices, however, and we are not aware of any systematic study of how these factors affect reliability estimates. This chapter describes studies that we conducted to provide such information.

We considered how the solder material, the fatigue life model parameters, the solder joint geometry, the use of volume-weighted averaging, and the parameters in the stress-strain model affect the expected number of cycles to failure (CTF) when using commercially available FEA software such as ANSYS. Our results show the inelastic strain energy density can be affected by the preferences of simulation methodology. Moreover, the limitations of some fatigue models are pointed out and the recommendations are provided for the engineers. These results will help engineers make better decisions when using modeling to support durability evaluation.

4.2 Approach

To support the reproducibility of our work, we used a PCB design from IPC-DPMX (IPC-2581), the online digital product model exchange that is a generic standard for the printed circuit

board and assembly manufacturing description data. The test case for our study was IPC-2581 B Test Case 3 board design [69] with BGA168 component from ANSYS Sherlock part library. ANSYS Sherlock is a physics-based reliability tool that provides life predictions for the electronics at the component, board, and system levels. The detailed information of the dimensions and material properties are listed in Table 6 and Table 7.

Table 6 Parameters of the BGA168 component

Balls	Ball matrix	Pitch	Component size	Ball diameter	Ball height	Ref
168	13×13 Full	1 mm	13.5 × 13.5 mm	0.645 mm	0.3 mm	BGA168

Table 7 Mechanical properties of materials in BGA168 assembly

Component	Young's modulus (GPa)			CTE (ppm/°C)			Poisson's ratio			Shear modulus (GPa)		
	E_x	E_y	E_z	α_x	α_y	α_z	ν_{xy}	ν_{xz}	ν_{yz}	G_{xy}	G_{xz}	G_{yz}
SAC305	39.99			22.28			0.36			14.70		
Component [69]	25.08			9.70			0.20			10.43		
PCB [69]	25.95	25.95	7.05	18.32	18.32	57.53	0.15			11.28		

We also considered different changes to a FEA model of the BGA168 component, its solder joints, and the PCB. We used different geometries for modeling the solder balls, different values for the volume-weighted averaging, and different constants for the stress-strain model. We first

created a FEA model with ANSYS Mechanical APDL because it provides the flexibility to adjust the mesh. In the FEA model, the geometry of solder joint was built in ball-, cube-, and frustum-shape, so three models with different solder joint geometries were employed in this chapter. The comparison flow was shown in Figure 7.

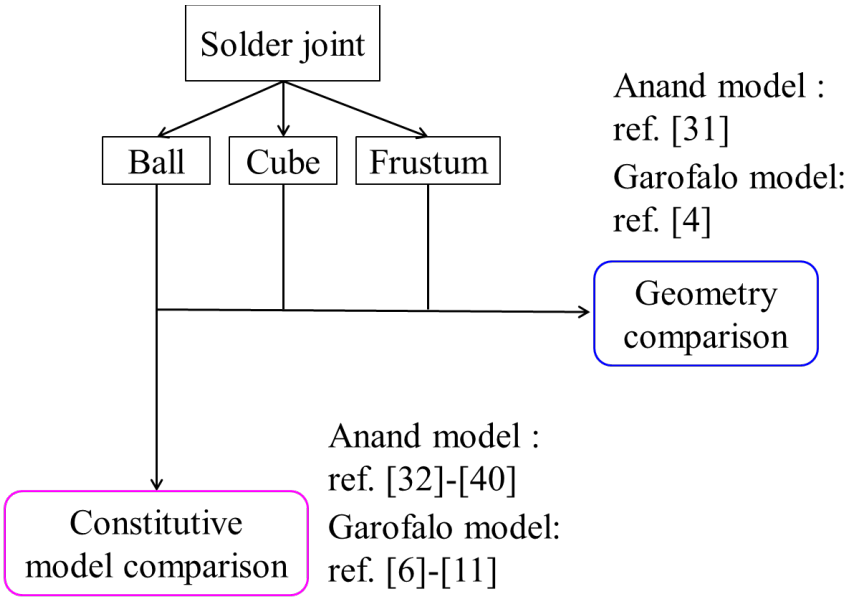

Figure 7 A schematic of the simulation flow between various models and geometries

In our approaches, step 1 was to make the simulation plan according to the constitutive models of solder material. Step 2 was to create a FEA model with ANSYS Mechanical APDL because it provided the flexibility to adjust the mesh of solder joints. In the FEA model, the geometry of solder joint was built in ball-shape. We then imported the FEA models into ANSYS Workbench for the FEA simulations. In order to consider the impact of the volume-weighted averaging technique, the number of temperature cycles, and the constitutive equations, we conducted

multiple simulation runs using different combinations of values for these factors, as shown in step 3 and step 4. Each simulation run yielded a value for the strain energy density ΔW with corresponding solder joint volume fraction, number of temperature cycles, and constitutive constants, as addressed in step 5. In the end, step 6 analyzed the variation of the cycles to failure prediction among the fatigue models. A schematic flowchart of the sequence of approaches is shown in Figure 8. The results are given in the next section.

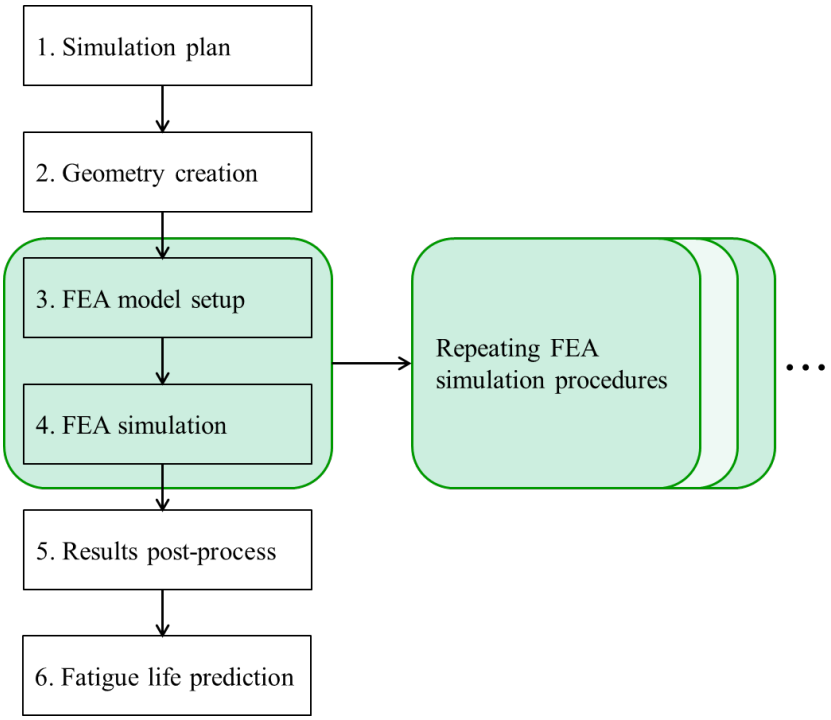

Figure 8 A schematic of the sequence of approaches

This process provided insights into how these factors affected the simulated strain energy density in both qualitative and quantitative way. The fatigue models mentioned in Table 1

determined the strain energy density according to their own preferences from the simulation results, so the predictions of the fatigue models should be normalized before comparing them together.

Many factors can affect the values of strain energy density, which are chosen as the inputs into the fatigue model, including the scope of volumes for volume-weighted averaging, the selection of the cycles for strain energy density accumulation, the selection of the parameters for inelastic constitute relationships, and the choice of material properties for FEA simulation. While manipulating the abovementioned factors, the available fatigue models from the literatures can be fairly reviewed and compared. On the other hand, all the materials used in the FEA simulation were considered as linear elastic and isotropic substances under the temperature cycling conditions. However, solder materials and PCB were excepted because solder materials performed as inelastic substances and PCB was orthotropic material.

In order to have a consistent comparison between the three geometries of solder ball, the volume was assigned to be close (within 0.3% deviation) between the geometries while keeping the same ball height. The volume calculation of the ball-shape and frustum-shape solder joint were determined by the following Equation (4.1) and (4.2). Figure 9 provides the schematic of the parameters of the geometry. For the cube-shape solder joint, the width and the height of the cube was 0.55 mm and 0.3 mm, respectively. For the ball-shape solder joint, the parameter R and h were 0.645 mm and 0.1725 mm, respectively. For the frustum-shape solder joint, the parameter *A1*, *A2*, and *h* were 0.25 mm^2, 0.36 mm^2, and 0.15 mm, respectively.

$$V_{Ball} = \frac{4}{3}\pi R^3 - \frac{2}{3}\pi h^2(3R - h) \tag{4.1}$$

$$V_{Frustum} = \frac{h}{3}\left(A1 + A2 + \sqrt{A1A2}\right) \tag{4.2}$$

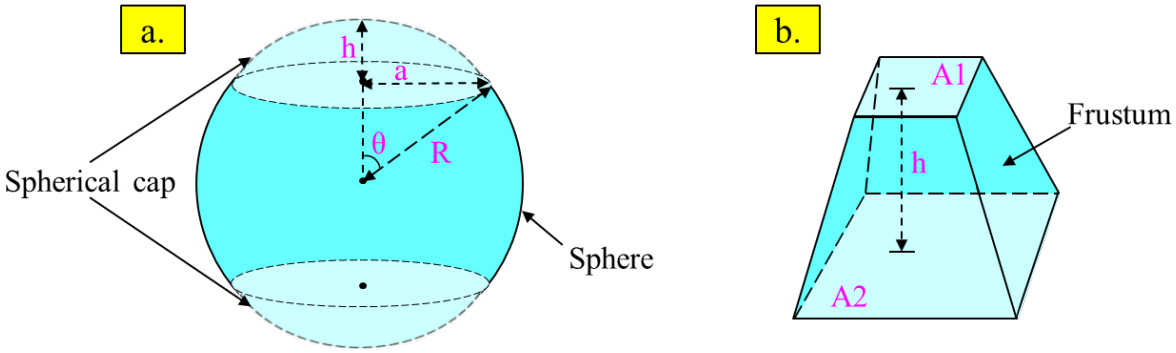

Figure 9 A schematic of the parameters of solder geometry: (a) Ball-shape (b) Frustum-shape

After the values of the geometry parameters were decided, the geometry of the FEA model was generated in ANSYS Mechanical APDL. Moreover, due to the nature of symmetry on the in-plane dimensions of the component, solder joints, and PCB, a quarter model of the FEA geometry was built to save the computational costs; the corresponding meshes are shown in Figure 10. We specified the solder material as SAC305.

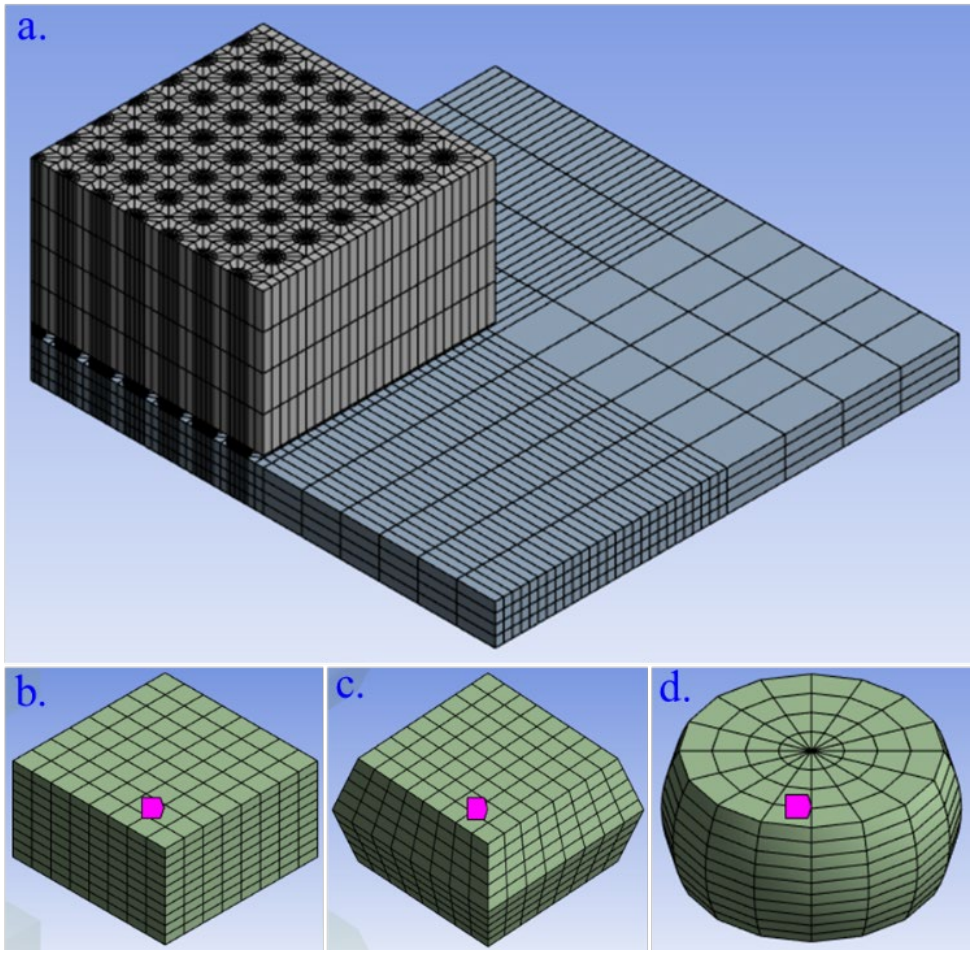

Figure 10 Finite element meshes of BGA168 component and the PCB: (a) isometric view of the quarter model; (b) cube geometry; (c) frustum geometry; (d) ball geometry

The strain energy density was determined with the volume-weighted averaging technique [17], which can use only a fraction of the elements in the calculation. We conducted simulations with different values for this fraction: 0.23% (critical element), 9%, 18%, 50%, and 100% for ball and frustum geometry. For cube geometry, the volume ratios were 10%, 20%, 50%, and 100%.

The corresponding volumes are shown in Figure 11. The information of the volumes was obtained from ANSYS Workbench by inserting a Volume result object in the Solution.

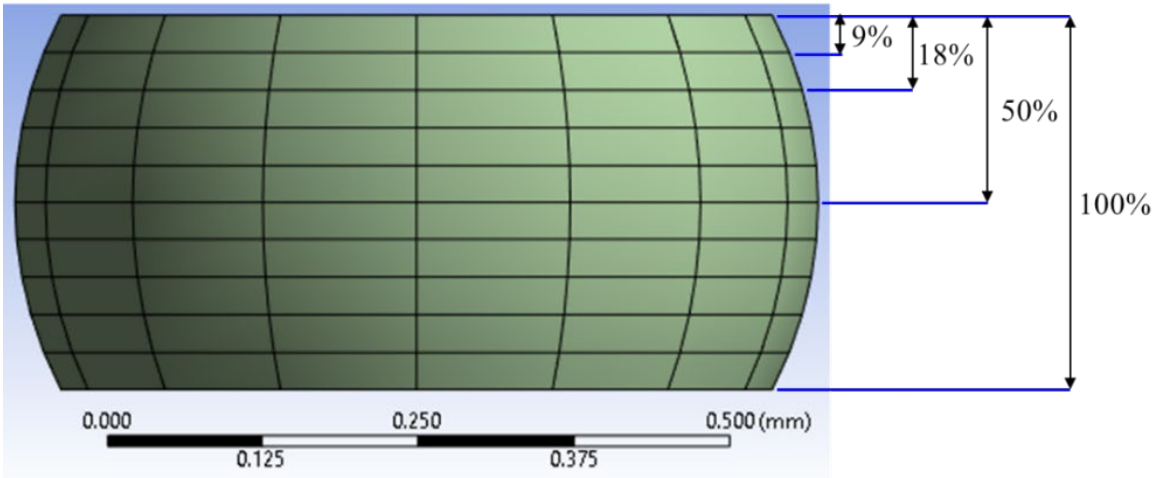

Figure 11 A schematic of the number of elements selected for volume-weighted averaging technique

The cycles chosen for the accumulation of strain energy density can also affect the fitting of the constants of fatigue model. Figure 12 showed the temperature cycling profile used in this study. In our study, the increment of strain energy density was obtained by taking the accumulation at Cycle 4. The value of this strain energy density accumulation (ΔW) can vary from cycle to cycle. Therefore, we also examined the impact of using Cycle 1, Cycle 2, and Cycle 3 accumulation to determine ΔW.

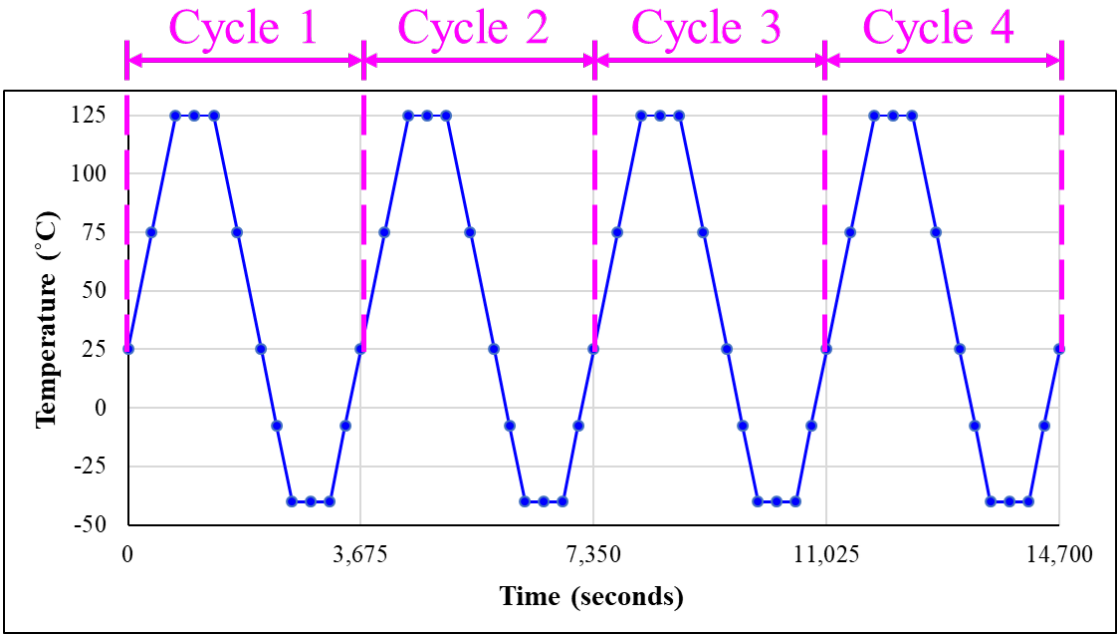

Figure 12 Temperature cycling profile used in this study

For the purpose of comparison on the effect of solder joint geometry, one set of constants from both Anand model and Garofalo-Arrhenius model were chosen to analyze the distribution of strain energy density accumulation. The remaining sets of the Anand and Garofalo-Arrhenius model were only applied for the ball-shaped solder joint to compare the variation among the models. These values are listed in Table 4 and Table 5.

Combing the abovementioned factors, the conditions of running simulations for ball-shape solder joint were summarized in Table 8. Our experiments employed a full factorial design, so there were 6×5×4 = 120 combinations for the subsequent analysis.

Table 8 Conditions for the factors of experiment design

Factor name	Level 1	Level 2	Level 3	Level 4	Level 5	Level 6
Constitutive model	GA01	GA02	GA03	GA04	GA05	GA06
Volume-weighted %	0.23%	9%	18%	50%	100%	---
Cycle accumulation	Cycle 1	Cycle 2	Cycle 3	Cycle 4	---	---

4.3 Results

The simulation results were summarized according to the solder volume and the simulated cycle, as addressed in Section 4.2, in order to pull out the necessary information for the comparison among the constitutive models and fatigue models. Figure 13 presented the strain energy density accumulation with elapsed time from Cycle 1 to Cycle 4 as well as the increment trend of the five solder volumes. As expected, the 0.23% solder volume (single element with maximum strain energy density) showed much higher value of the strain energy density than the other four volumes did.

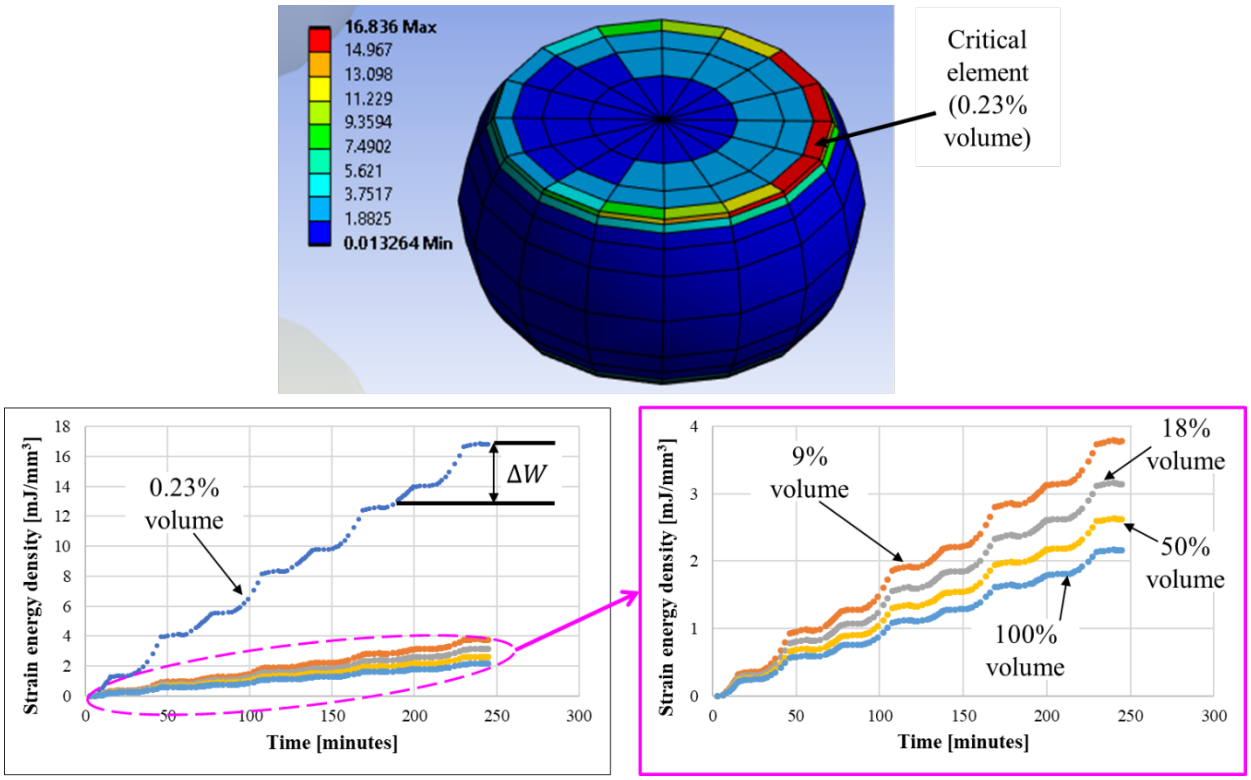

Figure 13 Elemental strain energy density accumulation with various volume-weighted averaging ratios

Figure 14 demonstrated the contribution of the solder joint geometry on the strain energy density accumulation. For both viscoplastic and creep only strain energy density, all three geometries exhibited close relationships among different cycles or volume-weighted amount.

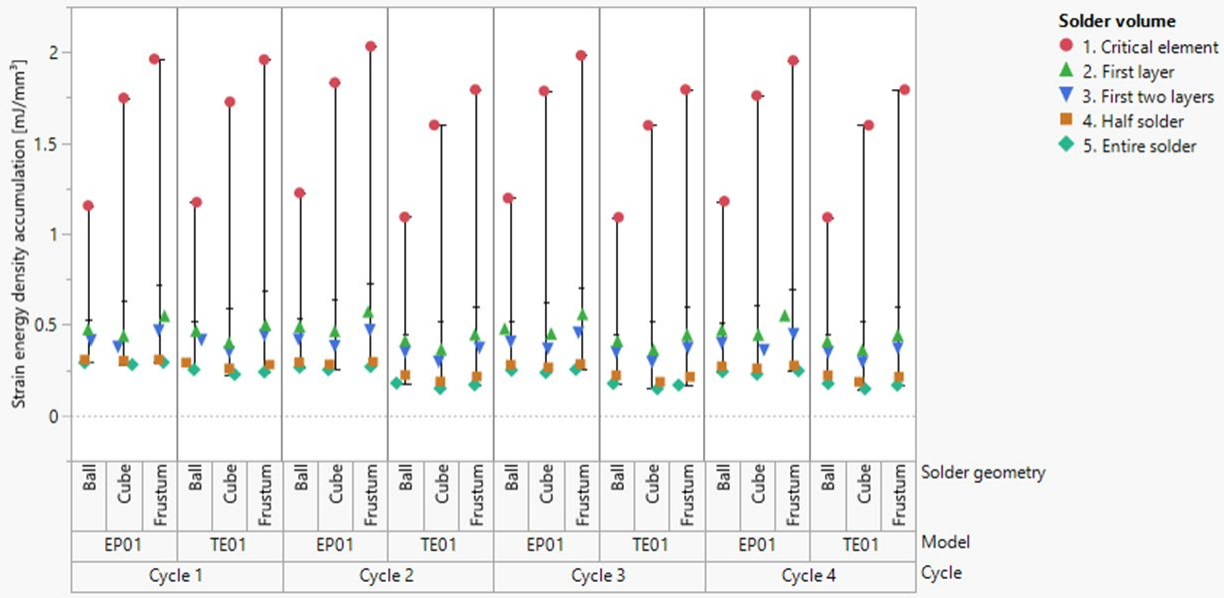

Figure 14 Solder joint geometry comparison

We used SAS JMP software to create variability charts (Figure 15 and Figure 16) to summarize the strain energy density data from all considered situations and to compare the data by constitutive models, strain energy density types, cycles, and solder volumes.

Figure 15 can be interpreted from various perspectives. First, there were significant differences on the group means between 0.23%, 9% and 18%, as well as 50% and 100% solder volumes. Second, the strain energy density accumulation exhibited different behaviors for viscoplastic and creep energies. For the creep energy type, the energy accumulation of Cycle 1 performed much lower means then Cycle 2 to 4 did. On the contrary, the viscoplastic energy type displayed similar strain energy density values from Cycle 1 to 4. Third, the strain energy densities of viscoplastic energy type was higher than the ones of creep energy type for all constitutive models. However, the difference between the viscoplastic and creep energy type was not consistent

among the models. Fourth, Student's t tests were conducted to compare the group means of each pair of the constitutive models for both viscoplastic and creep energy type. As shown in Figure 17 and Figure 18 , there were no significant differences discovered among the constitutive models and the group means of the viscoplastic strain energy densities exhibited close results.

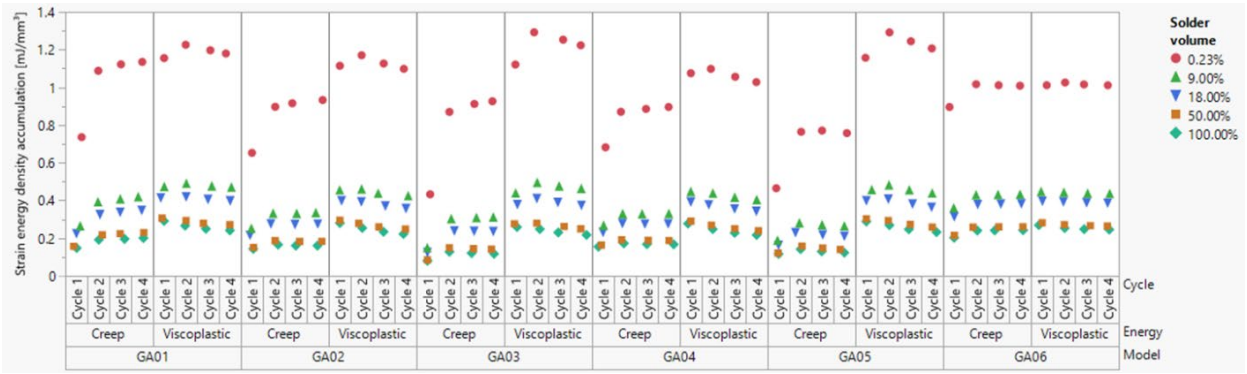

Figure 15 Variability chart of strain energy density with the selected Garofalo-Arrhenius models

Figure 16 provided similar information as Figure 15 did. First, the group means between 0.23%, 9% and 18%, as well as 50% and 100% solder volumes exhibited significant differences. Second, the strain energy density accumulation showed different relationships between the selected Anand models. The value of Cycle 1 accumulation can be either higher, lower, or equal to the accumulation of Cycle 2 to 4. Third, Student's t tests were also conducted to compare the group means of each pair of the Anand models, as shown in Figure 19. There were no significant differences discovered among the Anand models.

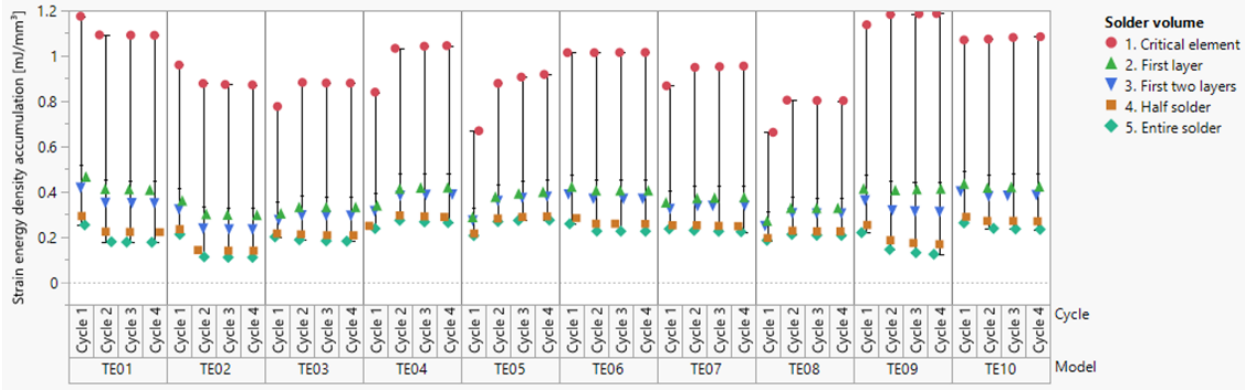

Figure 16 Variability chart of strain energy density with the selected with selected Anand models

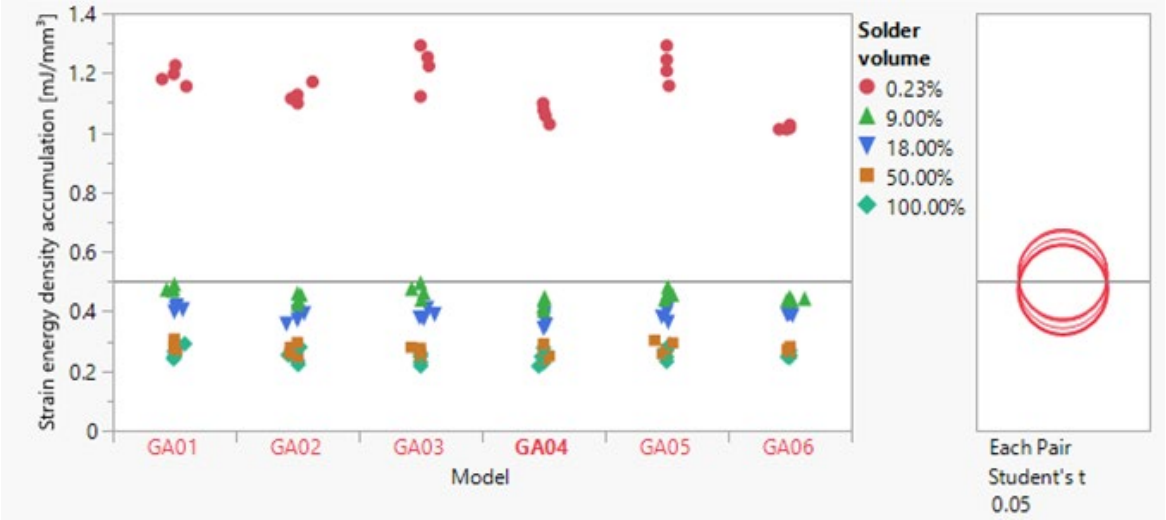

Figure 17 Group means comparison of energies among the Garofalo-Arrhenius models (Viscoplastic)

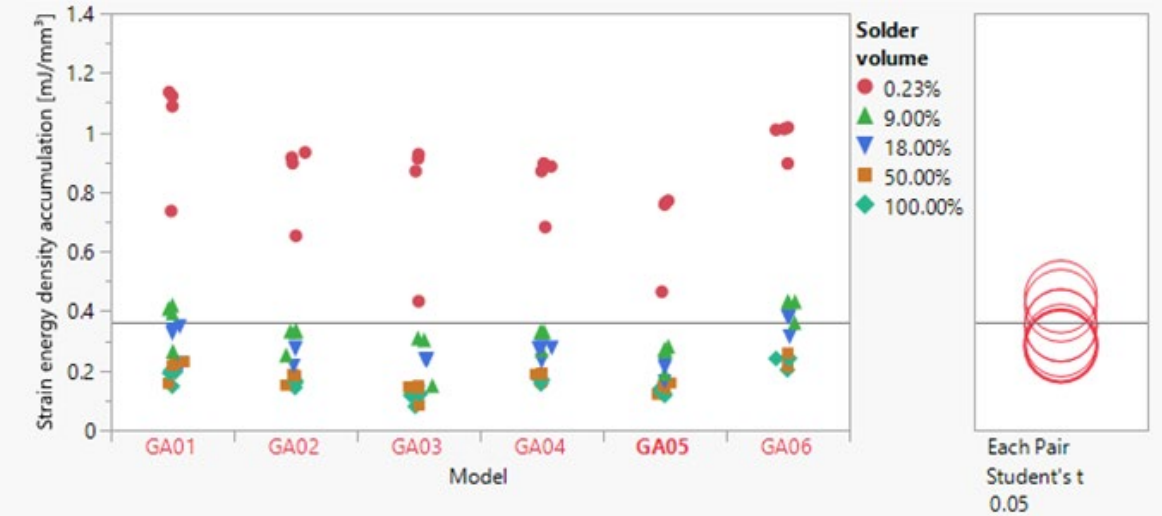

Figure 18 Group means comparison of energies among the Garofalo-Arrhenius models (Creep only)

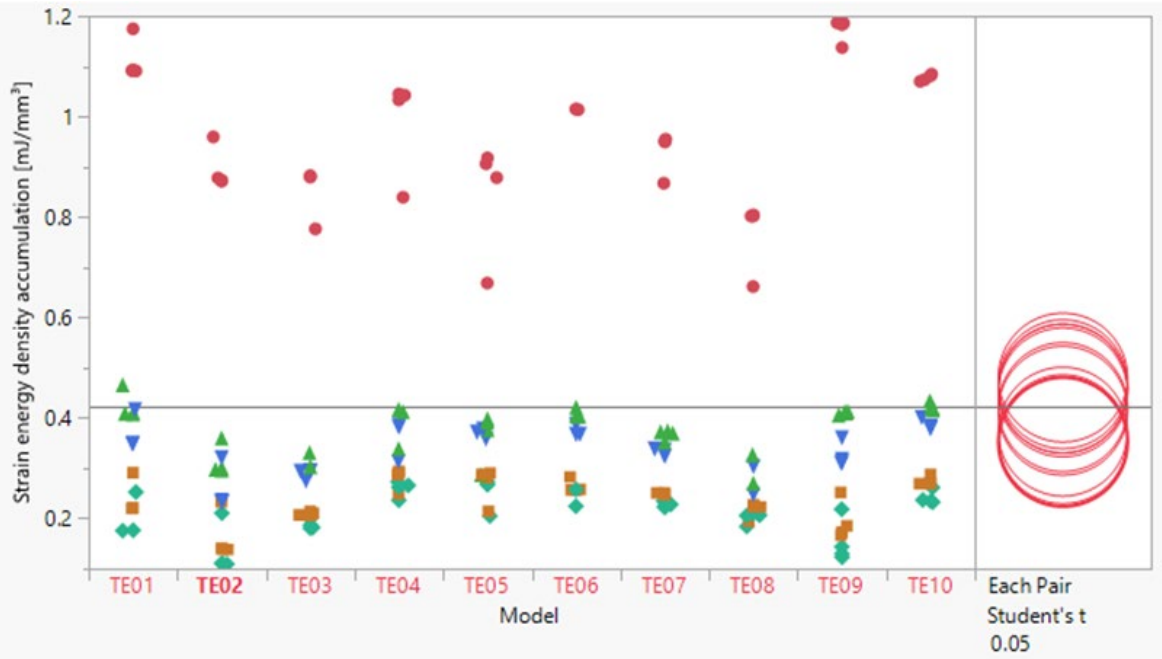

Figure 19 Group means comparison of energies among the Garofalo-Arrhenius models

4.4 Discussion

From Figure 15, the effect of cycle accumulation on the strain energy density variation could be ignored for 9% to 100% volume-weighted conditions. For the 0.23% volume (maximum element value) application, the strain energy density variation was around 3.7%. Fortunately, the fatigue models, which employed maximum element value, took cycle accumulation after Cycle 4 except Schubert et al. [6] didn't address the cycle accumulation, as shown in Table 9. Therefore, while comparing the fatigue models in this chapter, Cycle 4 accumulation was employed for the greater than three cycles and not specified situations.

Table 9 Strain energy density (ΔW) method from the selected fatigue life model studies

Authors	Constitute model	Volume-weighted amount	Cycle accumulation	ΔW range from literatures (mJ/mm^3)	ΔW from our simulations (mJ/mm^3)
Chen et al. [4]	GA01	8%	Cycle 4	0.10 to 0.15	0.47 (viscoplastic) 0.42 (creep)
Syed [5]	GA02	5.6%	Cycle 1 or 2	0.08 to 5.00	0.33
Schubert et al. [6]	GA02	100%	Not specified	0.05 to 2.00	0.22

Hsieh [7]	GA03	Maximum value (element)	Cycle 5	2.54 to 6.12	0.93
Hsieh and Tzeng [8]	GA04	Maximum value (element)	Cycle 5	5.90 to 7.20	0.90
Ghorbani and Spelt [9]	GA05	Maximum value (element)	Cycle 10	0.04 to 1.79	0.76
Sun et al. [10]	GA02	9.3%	Not specified (performed 3 cycles in simulation)	0.02 to 0.28	0.33
Zhang et al. [11]	GA06	5%	Cycle 3	0.05 to 0.40	0.44

In Table 9, five of the fatigue models directly described the amount of volume-weighted for the critical solder or the maximum value of the critical element (no volume-weighted) in their studies [6]−[9],[11]. The remaining fatigue models [4],[5],[10] only described the thickness or the layer(s) of elements used for the volume-weighted technique. In this situation, the values in Table 9 were determined by dividing the thickness of the layer(s) over the critical solder volume, which

was calculated from the figure in each literature. The volume of the critical element in each study was not possible to be approximated due to many reasons. Therefore, the 0.23% solder volume data was employed for the maximum element value. When the volume-weighted amount was less than 10%, the 9% solder volume data was applied for the subsequent comparisons because there should not exist a significant difference. Moreover, there were significant differences between the group means of 0.23%, 9%, and 100% solder volumes. For instance, the strain energy density of 0.23% volume was about 2.5 times higher than the one of 9% volume. Hence, the data from selected solder volume was critical while substituting into the fatigue models.

There was a significant difference on the group means between the viscoplastic energy group and creep energy group from the six studied Garofalo-Arrhenius models. Moreover, the difference between the viscoplastic energy and creep energy groups was not consistent among the six models. Therefore, the authors recommended to be consistent with the energy type while fitting the constants of Garofalo-Arrhenius model and to be careful of referring the available Garofalo-Arrhenius models from the literatures. Combining the considerations from the above three paragraphs, the strain energy density value needed to be adjusted before substituting it into the fatigue model. The strain energy density data from our simulations for each fatigue model situation was listed in Table 9.

Each fatigue model had specific combination of factors (as shown in Table 8) that could affect strain energy density calculation. For a given combination set, we found the ΔW by taking the accumulation of strain energy density from the cyclic strain energy density curve. Figure 20 presented the process flow to calculate the adjustment ratio of strain energy density for each fatigue model. We first chose one of the fatigue life models, which was Chen et al. [4] with viscoplastic

strain energy density, as the reference fatigue model A, ΔW_A. Then, for any of the other fatigue life models in Table 9, as the target fatigue model B. We repeated the simulation with the same temperature cycling profile, component, and PCB to get the target strain energy density, ΔW_B. For the creep constants of solder material, however, we used the values that were used in that study. Moreover, for each target fatigue life model, different settings of volume-weighted averaging amount and cycle accumulation was applied to determine the ΔW_B. Therefore, each fatigue life model had its own ΔW_B value. We then calculated the ratio R_B between each ΔW_B and the ΔW_A, as shown in Equation (4.3). For the comparison purpose, these ratios would be employed for the subsequent discussions of the predictions of cycles to failure.

$$R_B = \frac{\Delta W_B}{\Delta W_A} \tag{4.3}$$

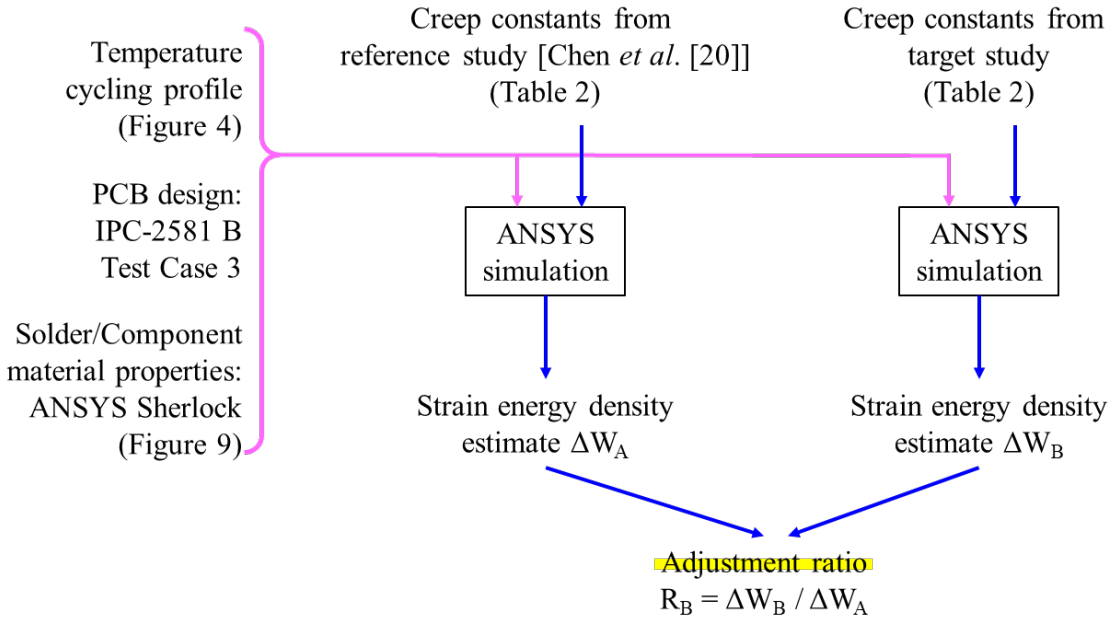

Figure 20 Strain energy density adjustment flow for the target studies

Figure 21 plotted the published values of strain energy density (ΔW) and cycles to failure (N_f) on a log-log scale. The range of ΔW and the fatigue coefficients and exponents were directly taken from the literature (listed in Table 1 and Table 9), and then the cycles to failures were determined by using them with the inverse power law in Equation (2.1) for each model from the literature. Most of the reported ΔW only covered a small range, and the value was less than 1 mJ/mm^3. However, this phenomenon could also reflect this small range might be a practical situation for modern electronic devices. For ΔW was greater than 2 MPa, fewer studies are available. Note that the strain energy density values are the results of simulations that used different sets of parameter values, and the cycles to failure values are different points (percentiles) from the empirical distributions collected by the different studies.

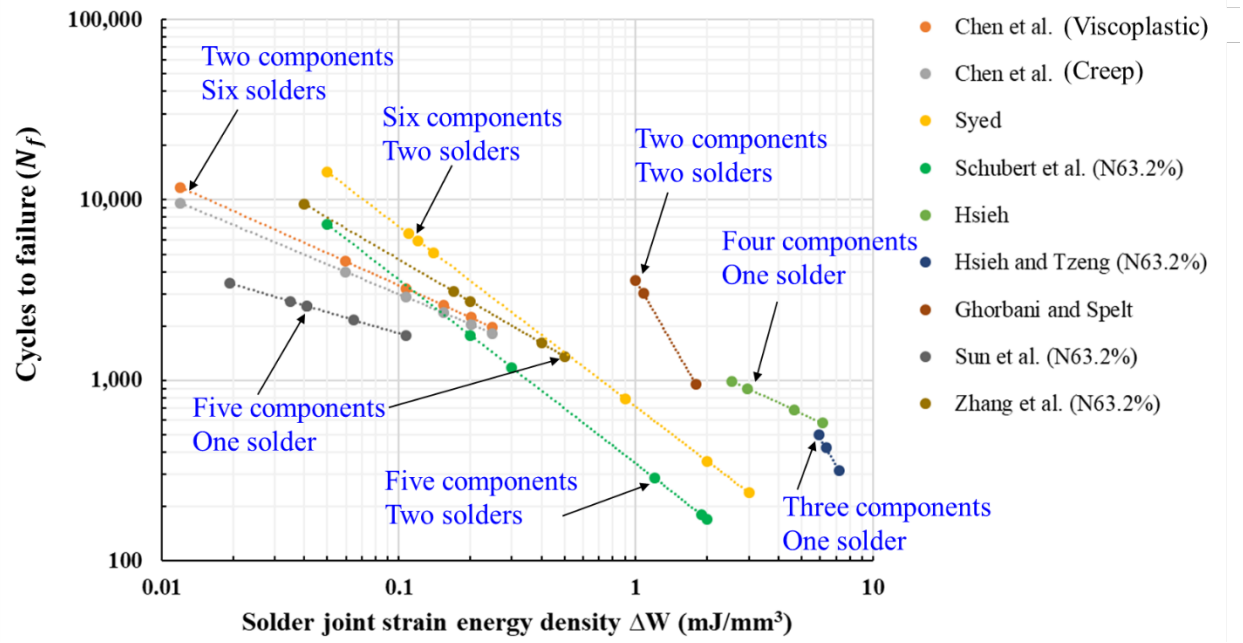

Figure 21 Distributions of strain energy density from the selected fatigue life models and their predictions on the cycles to failure

In order to have a consistent comparison for all the selected fatigue models, five strain energy density values were chosen based on all of the combinations of our simulation results, which were $\Delta W_i = \{0.09, 0.575, 1.06, 1.545, 2.03\}$ mJ/mm^3 for i = 1, 2, 3, 4, 5. These five values were used as the inputs of the fatigue models. Therefore, the predicted cycles to failure can be compared within the same strain energy density scope, as shown in Figure 22 and Figure 24.

The strain energy density value, ΔW_i, was multiplied by the adjustment ratio, R_B, before putting into the inverse power law, as shown in Equation (4.4), to get the adjusted strain energy density, $\Delta W_i'$, for each target fatigue life model, where i was from 1 to 8 due to total eight target models. After that, the cycles to failure (N_f) can be predicted with the adjusted strain energy density and the inverse power law with the corresponding coefficient and exponent from each target model, as presented in Equation (4.5).

$$\Delta W_i' = \Delta W_i \times R_B \tag{4.4}$$

$$N_f = (A_B \times \Delta W_i')^{n_B} \tag{4.5}$$

In Figure 22, the predicted cycles to failure followed the original assumptions in each fatigue life model. Thus, some of the cycles to failure produced mean life (N50%) predictions and the others pointed out the characteristic life (N63.2%).

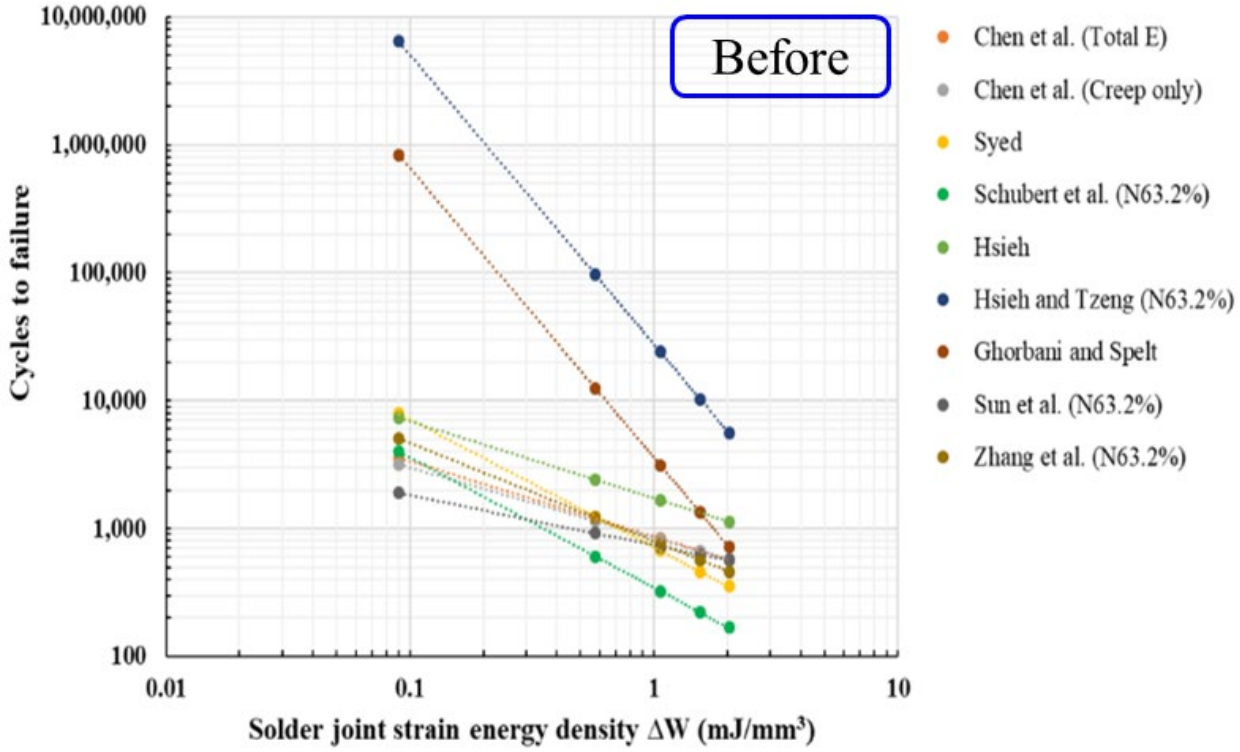

Figure 22 Distributions of strain energy density with selected ΔW range: Without ΔW and characteristic life (N63.2%) to mean life (N50%) adjustment

To have a more straightforward understanding on the predictions of all the selected fatigue models, the adjustment of life percentile was applied, as shown in Equation (4.6). N'_{fi} was referred to values that were derived from different ΔW_i. If the target model predicted mean life (N50%), N'_{fi} was the same as the N_f, which was the outcome of the inverse power law. On the other hand, if the target model predicted characteristic life (N63.2%), N_f was multiplied by $0.6931^{\left(\frac{1}{\beta_B}\right)}$ to get the adjusted N'_{fi}. β_B was the shape parameter of the two-parameter Weibull distribution from the

field failure data in each target fatigue life model. We averaged that study's published values of the shape parameter β to determine an aggregate β_B for that study.

$$N'_{fi} = N_f \text{ (if predicting mean life, N50\%)}$$
$$N'_{fi} = 0.6931^{\left(\frac{1}{\beta_B}\right)} N_f \text{ (if predicting characteristic life, N63.2\%)} \tag{4.6}$$

The ratio, $0.6931^{\left(\frac{1}{\beta_{Bi}}\right)}$, was simply a scaling factor from N63.2% to N50% in the Weibull distribution. Equation (4.7) to (4.10) showed the derivation of the ratio between mean life and characteristic life. The entire adjustment process flow for the cycles to failure prediction is shown in **Error! Reference source not found.**.

$$F(t) = 1 - e^{-\left(\frac{t}{\eta}\right)^{\beta}} \tag{4.7}$$

$$t_1 = \eta;\ F(t) = 0.632 = 63.2\%\ (characteristic\ life) \tag{4.8}$$

$$F(t) = 50\%\ (mean\ life) = 0.5 = 1 - e^{-\left(\frac{t_2}{\eta}\right)^{\beta}};\ t_2 = 0.6931^{\left(\frac{1}{\beta}\right)} \times \eta \tag{4.9}$$

$$t_1 > t_2\ and\ t_2 = 0.6931^{\left(\frac{1}{\beta}\right)} \times t_1 \tag{4.10}$$

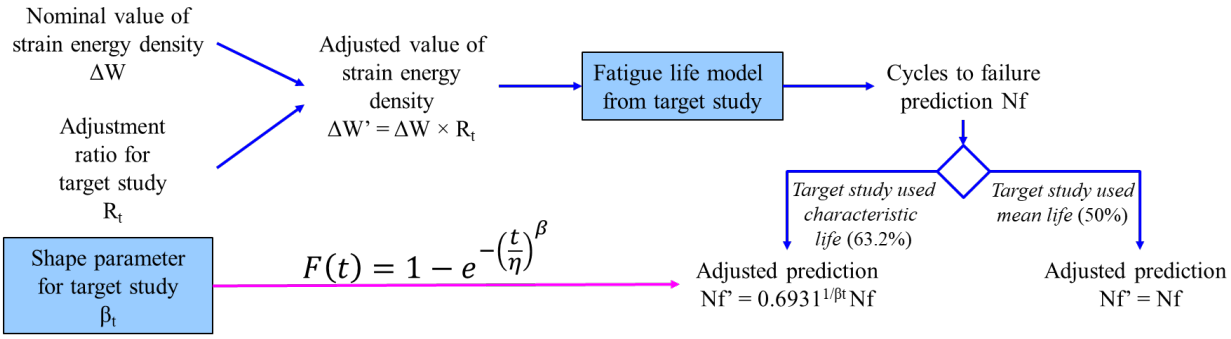

Figure 23 Process flow of the adjusted prediction of fatigue model

Therefore, the adjusted cycles to failure predictions was shown in Figure 24. The distribution of the predictions on cycles to failure among the fatigue models was significantly reduced after applying the adjustments, and exhibited excellent consistency around 1 mJ/mm^3 strain energy density.

Two of the fatigue life models, Hsieh and Tzeng [8] and Ghorbani and Spelt [9], exhibited divergences from the other seven models (see Figure 24). Three factors were found that were responsible for the significant divergence. First, both models did not apply volume-weighted averaging technique for determining the strain energy density. They employed the maximum element value as the strain energy density (see Table 9). This could induce large variation on the strain energy density while changing the mesh size of the FEA model. Therefore, the adjustment method for the strain energy density (see Figure 20) may not be appropriate for these two models because their mesh sizes were obviously smaller than our mesh size. Second, these two models only used three data points while curve fitting the coefficient and exponent of the inverse power law. This was the minimum number of data points for curve fitting an inverse power law, so predictions that were based on values of ΔW outside the range of their data can deviate in a certain

amount. Third, the ΔW range selected by these two models was around 1 mJ/mm^3, which was too small comparing to the reported ΔW range (from 0.01 to 8 mJ/mm^3). Combining with the second point, the prediction of the cycles to failure with smaller ΔW values can produce a huge deviation from the other seven models. Hence, these two models performed like outliers among the total nine fatigue models and the reason was the contributions from combining the abovementioned factors.

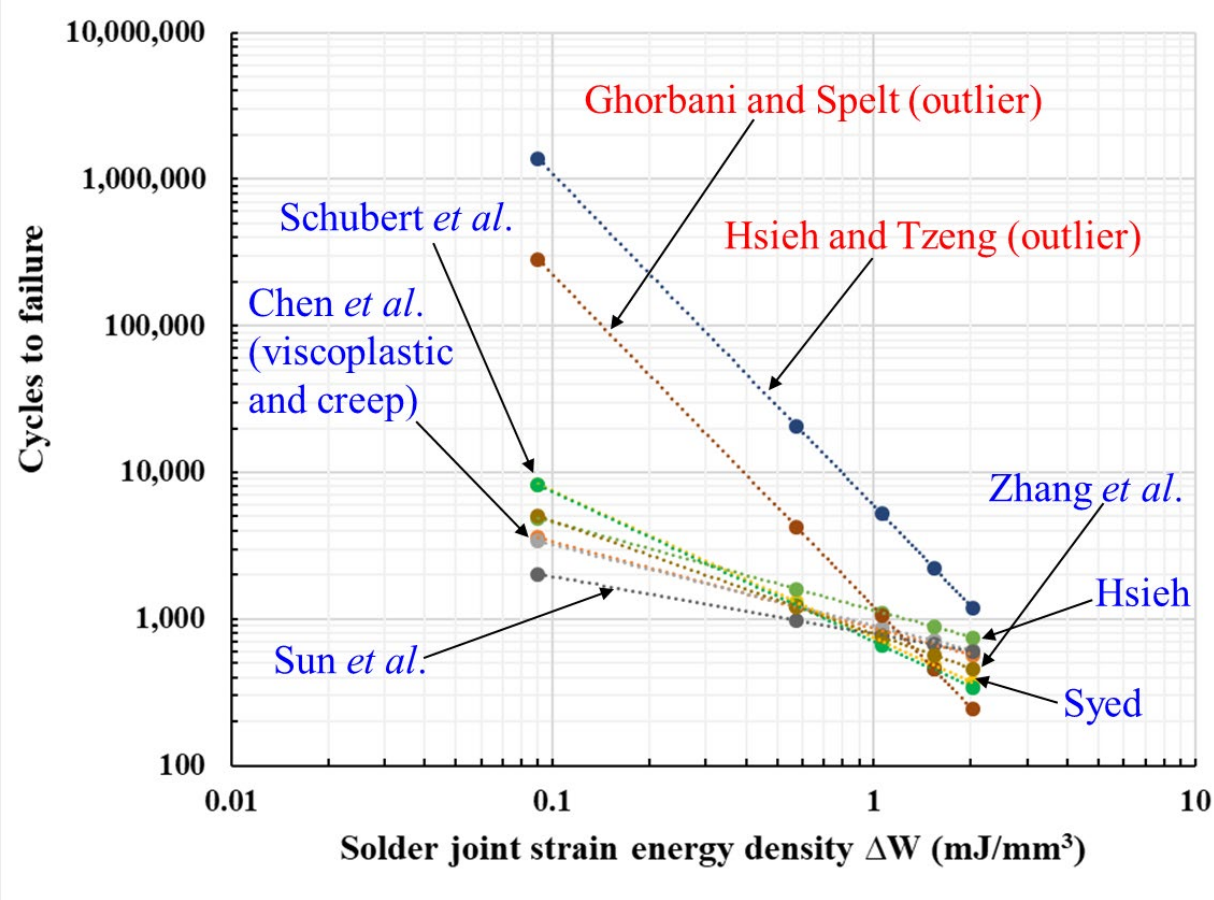

Figure 24 Distributions of strain energy density with selected ΔW range: With ΔW and characteristic life (N63.2%) to mean life (N50%) adjustment.

4.5 Summary

This chapter presented the results of a study of the solder joint reliability predictions from numerous low-cycle energy-based fatigue models in a prescribed strain energy density range. The nine selected fatigue models were built with their own solder materials, assemblies, simulation methodologies, and experiment conditions to predict mean life or characteristic life of the solder joint.

From the simulation perspective, the differences between the selected Garofalo-Arrhenius constitutive relationships from different solder materials were not significant on the accumulation of strain energy density. Other factors, including the amount of the critical solder for volume-weighted averaging technique, the selection of temperature cycle for strain energy density calculation, and the type of strain energy density (viscoplastic or creep), did make significant differences on the strain energy density accumulation. From the experiment perspective, the predicted cycles to failure (characteristic life or mean life) of the fatigue models were not consistent among the selected literature. Therefore, adjustment on the cycles to failure predictions was necessary after using the strain energy density as the input to the inverse power law equation.

In our studies, 0.23% volume (the critical element) exhibited significant differences of the strain energy density from different temperature cycles and other four solder volumes. For example, the strain energy density of 0.23% volume was about 2.5 times higher than the one of 9% volume. On the other hand, the difference of the group means between viscoplastic and creep

strain energy density was around 28%. In the end, the average mean life was about 94% of the average characteristic life with the shape parameter 6.04.

Combining the abovementioned adjustments with our own simulation results, the strain energy density range (0.09 to 2.03 mJ/mm^3) with five data points was chosen as the inputs of the selected fatigue models. The distribution of the predictions on cycles to failure among the fatigue models was significantly reduced after applying the adjustments, and exhibited excellent consistency around 1 mJ/mm^3 strain energy density. Two of the fatigue models showed large deviations from the other models especially for small strain energy density (less than 1 mJ/mm^3).

Three factors that could cause these large deviations were concluded. First, both of the two outlier models only employed three data points for curve fitting procedure. This can induce more deviation on the prediction of cycles to failure comparing to the model curve fitted with more data points. Second, the range of strain energy density for both two models was around 1 mJ/mm^3, which was smaller than the range of the values in the other studies. Moreover, all the strain energy densities of these two deviated fatigue models were larger than 1 mJ/mm^3 and some of them were larger than 5 mJ/mm^3. Therefore, the fittings of these two models were actually extrapolation for small strain energy densities, such as less than 0.1 mJ/mm^3. Third, both outlier models did not apply the volume-weighted averaging technique while determining the strain energy density. They used the maximum value of the strain energy density from a single element. This behavior could cause a large variation on the strain energy density value because of the mesh size of the FEA model. In general, the mesh size between this dissertation and their studies were different, so this could affect the outcome of our adjustment method. In the end, these three factors can be treated

as the precautions for the engineers no matter they are going to use these selected fatigue life models or to develop their own fatigue models.

Using a diverse set of fatigue models (such as those considered in this dissertation) will yield a range of results that may provide some insights that reduce (but do not eliminate) the uncertainty about how the new solder will impact reliability. In some cases, despite the uncertainty, the results may provide enough evidence to show that the reliability remains adequate; in other cases, the results will show that the reliability will be inadequate.

Chapter 5: Uncertainty Propagation for Reliability Prediction

This chapter is organized as follows. In Section 5.1, the need of developing an uncertainty propagation method for solder joint durability prediction is addressed. Section 5.2 presents the approach that we used. Section 5.3 presents the results of the EDR method, and Section 5.4 discusses those results. Section 5.5 concludes the paper.

5.1 Introduction

Among the many failure mechanisms of printed circuit boards (PCBs), the fatigue failure of the solder joints between the electronic components that are attached to the PCB and the PCB itself is a significant concern, especially for ball grid array (BGA) components [70].

Board-level temperature cycling tests have been used as one of the qualification criteria during the development of electronic components [71]. The cycles to failure under specific temperature cycling condition can be employed to calculate practical cycles to failure in the field by the inverse power law, as shown in Equation (2.1). However, the process time of qualification step can take more than six months. In order to save time and resources, the engineers would like to know an approximate distribution of the cycles to failure of the solder joints before conducting the temperature cycling qualification.

Finite element analysis (FEA) simulation is a convenient tool to estimate damage metrics, including inelastic strain and strain energy density of the critical solder, in a short time. Combining with the corresponding fatigue model of solder joints, the prediction of cycles to failure on the solder joints between the electronic component and PCB can be estimated without any temperature cycling testing [4].

To get the distribution of the predicted cycles to failure of solder joints, the distribution of the input of fatigue model needs to be addressed first. In the study that this chapter describes, the strain energy density accumulation was used as the damage metric to input the fatigue model. Many uncertainties can affect the FEA simulation results on the strain energy density accumulation, including the material properties and geometries [51]. Fortunately, most uncertainties can be treated as continuous distribution, such as normal distribution.

The eigenvector dimension reduction (EDR) method was proposed by Youn *et al*. [72] to handle the extensive computational costs induced by a large number of input variables. We applied the EDR method to determine the statistical moments of the probability density function (PDF) of the system response (strain energy density accumulation). The EDR method employs additive decomposition to calculate the statistical moments of the PDF, so it uses fewer simulation runs than other methods [72], such as response surface method (RSM) and Monte Carlo simulation (MCS). For instance, only 45 simulation runs are required when there are eleven uncertain input variables. While EDR method handles the distribution of the strain energy density accumulation, the distribution of cycles to failure is estimated by putting in the strain energy density accumulation into the fatigue models.

5.2 Approach

The section describes our approach to determine the uncertainty of the prediction of the fatigue life (N_f) of the solder joint between a BGA component and PCB. Let N_f be the output of the fatigue model listed in Equation (2.1). In this paper, the input of the fatigue model is the strain energy density, which is also the system response in the EDR method. The strain energy density

is obtained from the FEA simulation, so the uncertainty propagation through the FEA simulation needs to be addressed. The following list points out the steps to determine the uncertainty of the strain energy density accumulation of the solder joint.

1. Build the FEA model for the simulations.
2. Determine the uncertainty (mean and standard deviation) of each input variable (X_1 to X_{11}).
3. Construct the covariance matrix for the variables.
4. Determine the eigenvalues and eigenvectors of the covariance matrix.
5. Determine the sample points based on the means of the input variables and the eigenvalues.
6. Run simulations for the sample points and collect the strain energy density at each one.
7. Estimate the statistical moments using Equations (5.13) to (5.17).
8. Determine the characteristics of the PDF of system response using Equations (5.18) to (5.21).
9. Construct the PDF of the strain energy density by the Pearson system, using Equations (5.22) and (5.23).

Step 1

The FEA model was built with public-accessible resources, including IPC-2581 online PCB design files and ANSYS Sherlock part library. ANSYS Sherlock is a commercial reliability prediction software for electronics. We selected the BGA168 component from Sherlock part

library and put it on the IPC-2581 B Test Case 3 board design [69]. The diameter and height of the solder ball were 0.645 mm and 0.3 mm, respectively. The material properties of the solder joint, component, and PCB are summarized in Table 10.

Table 10 Material properties summary

Material	Young's modulus (GPa)			CTE (ppm/°C)			Poisson's ratio			Shear modulus (GPa)		
	E_x	E_y	E_z	α_x	α_y	α_z	ν_{xy}	ν_{xz}	ν_{yz}	G_{xy}	G_{xz}	G_{yz}
SAC305	−0.022×T(˚C) + 43.7			22.28			0.36			−0.008×T+ 16.1		
Component [69]	25.08			9.70			0.20			10.43		
PCB [69]	25.95	25.95	7.05	18.32	18.32	57.53	0.15			11.28		

For the Young's modulus (Table 10), the multilinear isotropic hardening properties in Equation (5.1), and the Garofalo-Arrhenius creep constants in Equation (5.2), we referred values from Chen *et al.* [4]. The C_1 to C_4 constants of Garofalo-Arrhenius creep model were 6.07 s^{-1}, 0.18 MPa^{-1}, 2.3, and 6,710 K, respectively. The multilinear isotropic hardening properties were listed in Equation (5.1), where σ was the instantaneous stress, K and n_{pl} were temperature-dependent instantaneous plasticity material constants, and T was temperature (degrees Celsius).

$$\varepsilon_{pl} = \left(\frac{\sigma}{K}\right)^{\left(\frac{1}{n_{pl}}\right)}$$
$$K = 121.6 - 0.4T \tag{5.1}$$
$$n_{pl} = 0.29 - 0.00046T$$

$$\frac{d\varepsilon_{cr}}{dt} = C_1[\sinh(C_2\sigma)]^{C_3} e^{-C_4/T} \tag{5.2}$$

Due to the geometric symmetry of the FEA model on the x-axis and y-axis, we employed a quarter model to run the simulations in order to save computational resources. Figure 25 exhibits the FEA model that we used in ANSYS Workbench with finite element meshes.

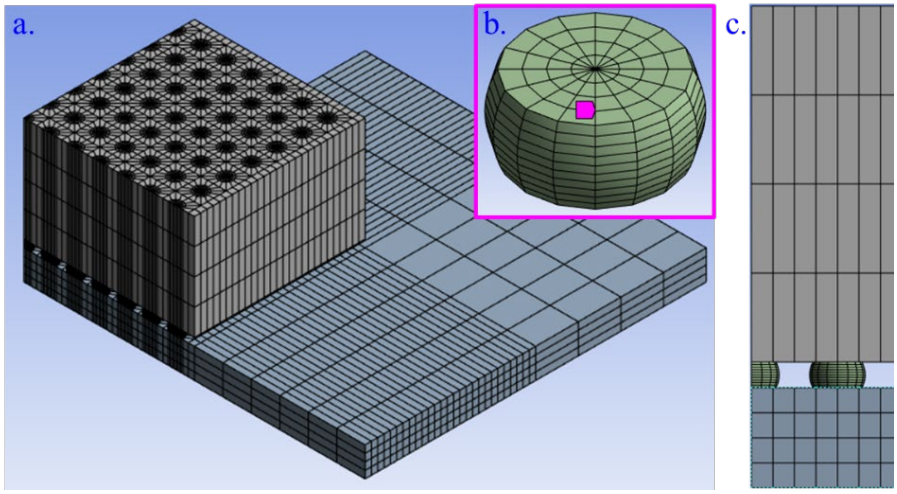

Figure 25 The quarter FEA model: (a) isometric view; (b) solder ball; (c) side view for component, ball, and PCB

Step 2

For a simple BGA and PCB assembly, the uncertain input variables that can affect the strain energy density (system response) can be determined from the fundamentals of mechanics theory. During temperature cycling, the strain energy density accumulated in the solder joint (ΔW) was related to the area under the shear stress−shear strain curve. Let $\Delta(\alpha\Delta T)$ be the thermal expansion differential. Let L_D be the length of the diagonal from solder joint to component center. Let h_s, A_s, and G_s be the height, cross-section area, and shear modulus of solder joint, respectively. Let E_1 and E_2 be the elastic modulus of the component and the PCB, respectively. Let A_1 and A_2 be the cross-section area of the component and PCB, respectively, perpendicular to the shear force (F). The value G_s can be determined from E_s and ν_s due to the shear modulus formula $G_s = E_s/[2(1+\nu_s)]$. The effects of A_1 and A_2 were simplified to their thickness only because of the simulation concern. Then, $\left[\frac{L_D}{E_1A_1}+\frac{L_D}{E_2A_2}+\frac{h_s}{A_sG_s}\right]^{-1}$ is the equivalent stiffness of the component, solder joint, and PCB. According to the shear strain formula and Hooke's law, the shear strain $\Delta\gamma$ and shear force F for a solder joint between the component and PCB can be determined using Equations (5.3) and (5.4), respectively.

$$\Delta\gamma = \frac{L_D}{h_s}\Delta(\alpha\Delta T) \tag{5.3}$$

$$F = \left[\frac{L_D}{E_1A_1}+\frac{L_D}{E_2A_2}+\frac{h_s}{A_sG_s}\right]^{-1}\Delta(\alpha\Delta T)L_D \tag{5.4}$$

The uncertain input variables that can affect the strain energy density accumulation of the solder joint between the component and PCB are summarized in Table 11. Eleven uncertain input variables were studied in this paper. Let μ_i be the mean value of the i-th random input variable. The mean value of X_1 to X_4 and X_6 to X_9 were referred to IPC-2581 B Test Case 3 board design [69] and the BGA168 component from ANSYS Sherlock part library. The mean value of X_5 was determined from Chen *et al.* [4]. The tolerances for X_1 and X_2 were determined from a supplier's website [73], and the tolerances for X_6 to X_9 were determined from Wei *et al.* [51]. We could not find appropriate tolerance value for X_3 to X_5, so we assumed 10% for these three variables. The standard deviation (σ) was determined by dividing the tolerance by three for all uncertain input variables.

Table 11 Uncertain input variables for a BGA component under temperature cycling (see text for sources of these values)

Variable	Physical meaning	Mean (μ_i)	Tolerance	Standard deviation (σ)
X_1	Solder ball height (mm)	0.3	7%	0.007
X_2	Solder ball diameter (mm)	0.645	7%	0.015
X_3	Solder ball CTE (ppm/˚C)	22.28	10%	0.743
X_4	Solder ball ν	0.36	10%	0.012
X_5	Solder ball E (GPa)	−0.022×T(˚C) + 43.7	10%	1.438 (T=25 ˚C)
X_6	Component E (GPa)	25.08	5%	0.418
X_7	Component CTE (ppm/˚C)	9.70	20%	0.647
X_8	Component thickness (mm)	4.15	17%	0.235
X_9	PCB E_{xy} (GPa)	25.95	5%	0.433
X_{10}	PCB CTE (ppm/˚C)	18.32	15%	0.916
X_{11}	PCB thickness (mm)	1.168	23%	0.090

Step 3

After the uncertainty of the uncertain input variables were defined, the covariance matrix was built according to the relationship between each pair of variables. The first thing was to examine the correlation between the variables.

The distribution of X_1 and X_2 was assumed as a bivariate normal distribution due to the correlation between X_1 and X_2. If the volume is fixed, the relationship between X_1 and X_2 is negatively correlated. The volume calculation of the solder joint was shown in Equation (5.5) and the schematic of the parameters of the geometry was provided in Figure 26. The data points of ball diameter and ball height with fixed ball volume were presented in Figure 27. Therefore, the correlation coefficient (ρ) was calculated by utilizing Equation (5.6) and the data points in Figure 27, and the value was around −0.9838.

$$V_{Ball} = \frac{4}{3}\pi R^3 - \frac{2}{3}\pi h^2(3R - h) \tag{5.5}$$

$$\rho = \frac{\sum(x_i - \bar{x})\,(y_i - \bar{y})}{\sqrt{\sum(x_i - \bar{x})^2 \sum(y_i - \bar{y})^2}} \tag{5.6}$$

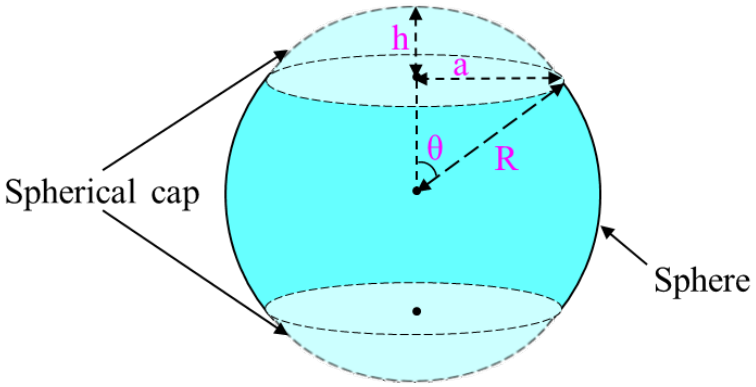

Figure 26 A schematic of the parameters of solder ball

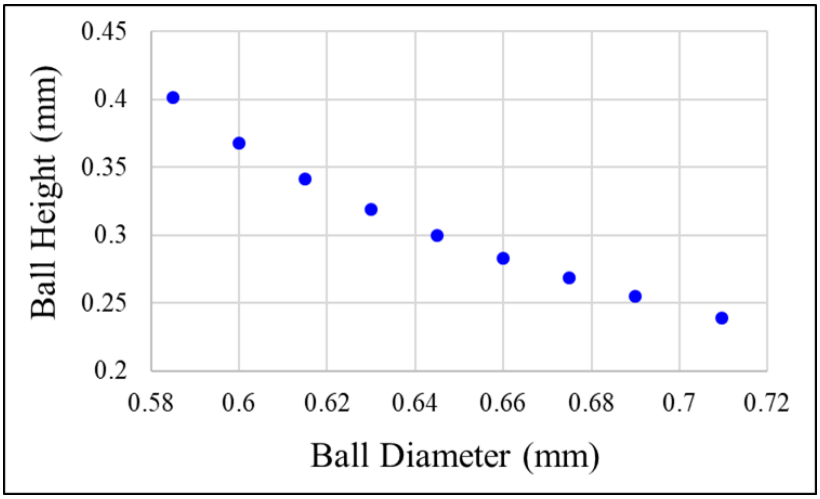

Figure 27 Correlation between ball diameter and ball height with fixed ball volume

On the other hand, the distribution of X_3 to X_9 was assumed as a normal distribution and was not correlated to each other. Hence, the correlation coefficient was zero between theses uncertain input variables. The next step was to build the covariance matrix for all nine uncertain input

variables. The equation of calculating the covariance between any two variables was shown in Equation (5.7).

$$Cov(A,B) = \sigma(A)\sigma(B)\rho(A,B) \tag{5.7}$$

The covariance of each pair of the eleven uncertain input variables was calculated and then put in the covariance matrix, as shown in Equation (5.8). The element on the diagonal of the matrix was the variance of the input variable itself, which was σ_i^2. Moreover, Cov_{ij} and Cov_{ji} were equivalent in the matrix.

$$Cov_{ij} = \begin{bmatrix} \sigma_1^2 & \cdots & Cov_{1N} \\ \vdots & \ddots & \vdots \\ Cov_{N1} & \cdots & \sigma_N^2 \end{bmatrix}$$

$$= \begin{bmatrix} 0.007^2 & -1.04\times10^{-4} & 0 & 0 & 0 & 0 & 0 & 0 & 0 & 0 & 0 \\ -1.04\times10^{-4} & 0.015^2 & 0 & 0 & 0 & 0 & 0 & 0 & 0 & 0 & 0 \\ 0 & 0 & 0.743^2 & 0 & 0 & 0 & 0 & 0 & 0 & 0 & 0 \\ 0 & 0 & 0 & 0.012^2 & 0 & 0 & 0 & 0 & 0 & 0 & 0 \\ 0 & 0 & 0 & 0 & 1.438^2 & 0 & 0 & 0 & 0 & 0 & 0 \\ 0 & 0 & 0 & 0 & 0 & 0.418^2 & 0 & 0 & 0 & 0 & 0 \\ 0 & 0 & 0 & 0 & 0 & 0 & 0.647^2 & 0 & 0 & 0 & 0 \\ 0 & 0 & 0 & 0 & 0 & 0 & 0 & 0.235^2 & 0 & 0 & 0 \\ 0 & 0 & 0 & 0 & 0 & 0 & 0 & 0 & 0.433^2 & 0 & 0 \\ 0 & 0 & 0 & 0 & 0 & 0 & 0 & 0 & 0 & 0.916^2 & 0 \\ 0 & 0 & 0 & 0 & 0 & 0 & 0 & 0 & 0 & 0 & 0.090^2 \end{bmatrix} \tag{5.8}$$

Step 4

By solving the eigenvectors and eigenvalues of the covariance matrix with Equation (5.9), the multi-dimensional integration of the joint PDF (eleven dimensions for $N = 11$ uncertain input variables) can be decomposed into eleven one-dimensional integrations according to the eigenvector of each random input variable. Equations (5.10) and (5.11) list the eigenvalues (λ_i) and eigenvectors (V_{ji}).

$$Cov_{ij}V_{ji} = \lambda_i V_{ji} \tag{5.9}$$

$$\lambda_i = \begin{bmatrix} 1.302 \times 10^{-6} \\ 2.757 \times 10^{-4} \\ 0.552 \\ 1.440 \times 10^{-4} \\ 2.122 \\ 0.175 \\ 0.418 \\ 0.055 \\ 0.187 \\ 0.839 \\ 0.008 \end{bmatrix} \tag{5.10}$$

$$V_{ji} = \begin{bmatrix} -0.909 & -0.417 & 0 & 0 & 0 & 0 & 0 & 0 & 0 & 0 & 0 \\ -0.417 & 0.909 & 0 & 0 & 0 & 0 & 0 & 0 & 0 & 0 & 0 \\ 0 & 0 & 1 & 0 & 0 & 0 & 0 & 0 & 0 & 0 & 0 \\ 0 & 0 & 0 & 1 & 0 & 0 & 0 & 0 & 0 & 0 & 0 \\ 0 & 0 & 0 & 0 & 1 & 0 & 0 & 0 & 0 & 0 & 0 \\ 0 & 0 & 0 & 0 & 0 & 1 & 0 & 0 & 0 & 0 & 0 \\ 0 & 0 & 0 & 0 & 0 & 0 & 1 & 0 & 0 & 0 & 0 \\ 0 & 0 & 0 & 0 & 0 & 0 & 0 & 1 & 0 & 0 & 0 \\ 0 & 0 & 0 & 0 & 0 & 0 & 0 & 0 & 1 & 0 & 0 \\ 0 & 0 & 0 & 0 & 0 & 0 & 0 & 0 & 0 & 1 & 0 \\ 0 & 0 & 0 & 0 & 0 & 0 & 0 & 0 & 0 & 0 & 1 \end{bmatrix} \quad (5.11)$$

Step 5

The eigenvector with the largest eigenvalue indicated the direction of the largest variation of the covariance matrix, and so on. On the other hand, the square root of the eigenvalue was the standard deviation of the variation along its corresponding direction. The sample points along each eigenvector were then chosen using multiples of the square root of the eigenvalue and the sampling scheme. We used five values for each random input variable along the direction of its eigenvector [72], which yielded five sample points (including the one with all of the mean values), as shown in Equation (5.12).

$$\begin{aligned} [V_i]_1 &= \left[\mu_1, \cdots, \mu_i - 3\sqrt{\lambda_i}, \cdots, \mu_N\right] \\ [V_i]_2 &= \left[\mu_1, \cdots, \mu_i - 1.5\sqrt{\lambda_i}, \cdots, \mu_N\right] \\ [V_i]_3 &= [\mu_1, \cdots, \mu_N] \\ [V_i]_4 &= \left[\mu_1, \cdots, \mu_i + 1.5\sqrt{\lambda_i}, \cdots, \mu_N\right] \\ [V_i]_5 &= \left[\mu_1, \cdots, \mu_i + 3\sqrt{\lambda_i}, \cdots, \mu_N\right] \end{aligned} \quad (5.12)$$

Thus, one sample point $[V_i]_3$ was the same for all of the input variables, while four of the sample points were specific for that input variable. Thus, we used the 4N+1 sampling scheme with 45 sample points. The values for each random input variable are provided in Table 12. Let Y_{ij} be the system response at sample point $[V_i]_j$.

Table 12 The values for each random input variable used for the sample points

Variable i	$\mu_i - 3\sqrt{\lambda_i}$	$\mu_i - 1.5\sqrt{\lambda_i}$	μ_i	$\mu_i + 1.5\sqrt{\lambda_i}$	$\mu_i + 3\sqrt{\lambda_i}$
X_1	0.297	0.298	0.300	0.302	0.303
X_2	0.595	0.620	0.645	0.670	0.695
X_3	20.05	21.17	22.28	23.39	24.51
X_4	0.324	0.342	0.360	0.378	0.396
X_5	−0.022T+39.33	−0.022T+41.52	−0.022T+43.70	−0.022T+45.89	−0.022T+48.07
X_6	23.83	24.45	25.08	25.71	26.33
X_7	7.760	8.730	9.700	10.67	11.64
X_8	3.44	3.80	4.15	4.50	4.86
X_9	24.65	25.30	25.95	26.60	27.25
X_{10}	15.57	16.95	18.32	19.69	21.07
X_{11}	0.4548	0.4647	0.4734	0.4817	0.4898

Step 6

After the sample points were determined, we used the values of the material properties and geometries (X_1 to X_{11}) as inputs to the FEA model, and we simulated the temperature cycling profile shown in Figure 28. The simulation was performed at the 45 sample points to get the corresponding strain energy densities. After the simulation runs, we calculated the strain energy density via the accumulation of Cycle 4 and the volume-weighted averaging technique [17], which used 9% of the solder joint volume to get the average strain energy density, as shown in Figure 29. These strain energy densities were the system responses for the EDR method addressed in the next step.

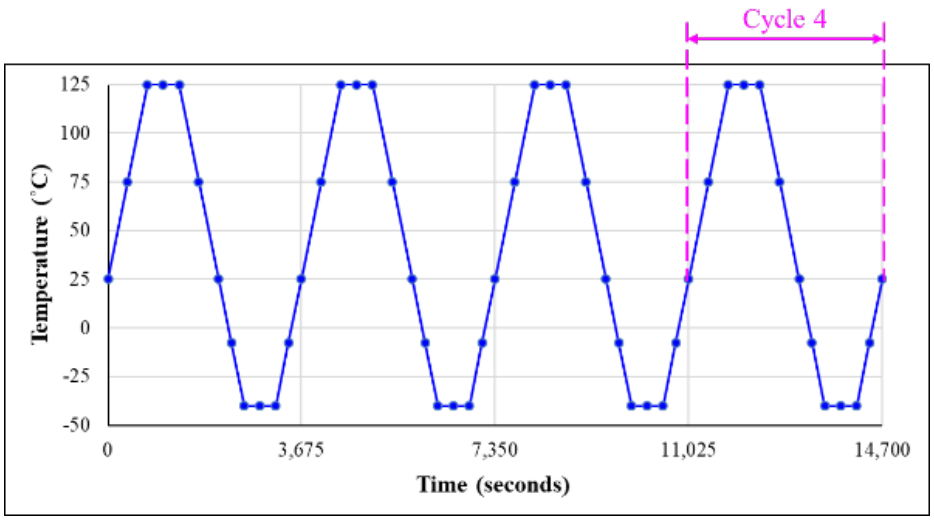

Figure 28 Temperature cycling profile

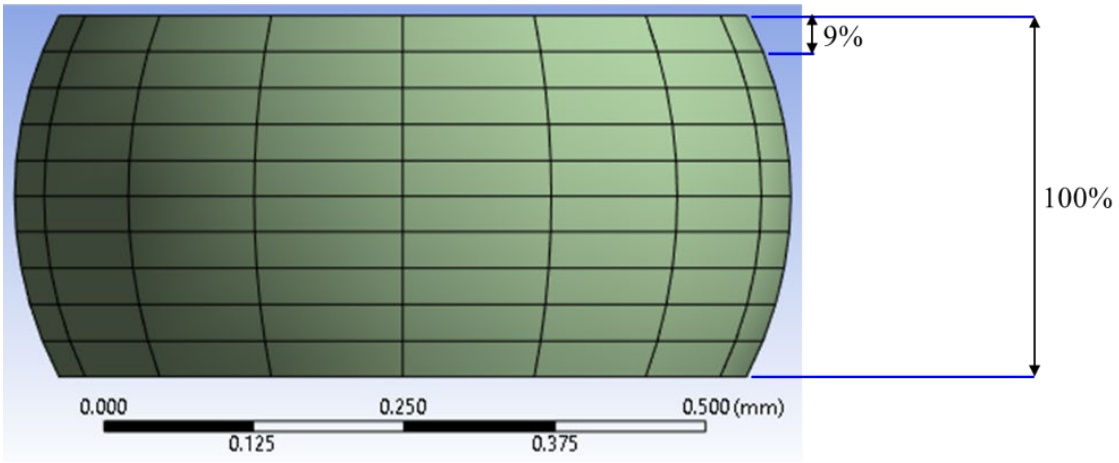

Figure 29 Fraction of the solder joint volume

Step 7

After obtaining the system responses from the simulations of the sample points, we employed the EDR method to calculate the statistical moments of the distribution of system response and then built the PDF of the system response by probability estimation methods, including the method of moments and Pearson system.

Let $E\{\ \}$ symbol be the expectation operator, and let, $X_1, \cdots, X_N$ be the N input variables. Let $Y(X_1, \cdots, X_N)$ be the system response. Let $f_{X_1,\cdots,X_N}(X_1, \cdots, X_N)$ be the joint PDF of the input variables. In general, the m-th order statistical moment of a distribution can be written as Equation (5.13), but this can be calculated using Equation (5.14) and the recursion shown in Equation (5.15) [51],[72].

$$E\{[Y(X_1,\cdots,X_N)]^m\} \equiv \int_{-\infty}^{+\infty} \cdots \int_{-\infty}^{+\infty} \{Y(X_1,\cdots,X_N)\}^m f_{X_1,\cdots,X_N}(X_1,\cdots,X_N)dX_1\cdots dX_N \quad (5.13)$$

$$E\{[Y(X_1,\cdots,X_N)]^m\} = \sum_{i=0}^{m} \frac{m!}{i!\,(m-i)!} S_N^i [-(N-1)\times Y(\mu_1,\cdots\mu_N)]^{m-i} \quad (5.14)$$

$$\begin{cases} S_1^i = \int_{-\infty}^{+\infty} \{Y(X_1,\mu_2,\cdots,\mu_N)\}^i \times f_{X_1,\cdots,X_N}(X_1|X_2=\mu_2,\cdots,X_N=\mu_N)dX_1 \\ S_j^i = \sum_{k=0}^{i} \frac{i!}{k!\,(i-k)!} S_{j-1}^k \int_{-\infty}^{+\infty} \{Y(\mu_1,\cdots,\mu_{j-1},X_j,\mu_{j+1},\cdots\mu_N)\}^{i-k} \\ \quad \times f_{X_1,\cdots,X_N}(X_j|X_1=\mu_1,\cdots,X_{j-1}=\mu_{j-1},X_{j+1}=\mu_{j+1},\cdots,X_N=\mu_N)dX_j \\ S_N^i = \sum_{k=0}^{i} \frac{i!}{k!\,(i-k)!} S_{N-1}^k \int_{-\infty}^{+\infty} \{Y(\mu_1,\cdots X_N)\}^{i-k} \\ \quad \times f_{X_1,\cdots,X_N}(X_N|X_1=\mu_1,\cdots,X_{N-1}=\mu_{N-1})dX_N \end{cases} \quad (5.15)$$

From Equation (5.13) to (5.14), many assumptions were made to deal with the multi-dimensional challenge in Equation (5.13). First, Rahman and Xu [74] decomposed the multi-dimensional response function $Y(X_1,\cdots,X_N)$ into several one-dimensional functions, as shown in

Equation (5.16). Second, the binomial formula can be applied to Equation (5.16) to approximate Equation (5.13) and then obtain Equation (5.14).

$$Y(X_1, \cdots, X_N) \approx \sum_{j=1}^{N} Y(\mu_1, \cdots, \mu_{j-1}, X_j, \mu_{j+1}, \cdots, \mu_N) - (N-1) \cdot Y(\mu_1, \cdots, \mu_N) \qquad (5.16)$$

We then used Equation (5.17) to approximate the one-dimensional integrations shown in Equation (5.15). As shown in Figure 30, the blue curve was the PDF of X_7 input variable. The area under the X_7 PDF can be approximated with the yellow blocks, which were the weights at each integration points. Let w_{ji} be the weight used at integration point $x_{j,i}$. Let $x_{j,i}$ be the i[th] integration point of the j[th] input variable, and the $w_{j,i}$ was the i[th] weight to approximate the area under X_j PDF from $\left[x_{j,i} - \frac{(x_{j,i} - x_{j,i-1})}{2}\right]$ to $\left[x_{j,i} + \frac{(x_{j,i+1} - x_{j,i})}{2}\right]$. In this study, we employed 21 integration points according to Youn *et al.*'s study [72], which discussed several nonlinear system response cases. The 21 integration points were assumed to be able to handle the strain energy density in this study.

In Figure 30, the red curve was the system response, which was the strain energy density, at X_7 direction. $Y(\mu_1, \cdots, \mu_{j-1}, x_{j,i}, \mu_{j+1}, \cdots, \mu_N)$ was the system response at the $x_{j,i}$ integration point with the means of the other input variables, as shown as black cross. The system response at EDR 4N+1 sample point was indicated as green dot.

Let $g_j(X_j)$ be the marginal distribution of X_j when the other input variables were fixed at their means, which was the blue curve in Figure 30. Therefore, Equation (5.17) was actually approximating the products between the blue curve and red curve with the black cross and yellow blocks.

$$g_j(X_j) = f_{X_1,\cdots,X_N}(X_j|X_1 = \mu_1, \cdots, X_{j-1} = \mu_{j-1}, X_{j+1} = \mu_{j+1}, \cdots, X_N = \mu_N)$$

$$\int_{-\infty}^{+\infty} \{Y(\mu_1, \cdots, \mu_{j-1}, X_j, \mu_{j+1}, \cdots \mu_N)\}^r g_j(X_j) dX_j \tag{5.17}$$

$$\cong \sum_{i=1}^{n} w_{j,i}\{Y(\mu_1, \cdots, \mu_{j-1}, x_{j,i}, \mu_{j+1}, \cdots, \mu_N)\}^r$$

While conducting the one-dimensional integration approximation, the EDR method can maintain the accuracy and reduce the number of FEA simulations under two major assumptions. First, the sampling scheme (4N+1 or 2N+1) proposed by the EDR method can handle the statistical correlation and variation of the input variables. As shown in Figure 30, the PDF value of X_7 input variable becomes extreme low when the value of X_7 is greater than $X_7 \pm 3\sqrt{\lambda_7}$. This situation actually significantly lessens their impact while performing the one-dimensional integration approximation. Second, five sampling points (4N+1 scheme) are required when the system response is tremendously nonlinear within $X_7 \pm 3\sqrt{\lambda_7}$ range because more sampling points are necessary to catch the nonlinear behavior of the system response.

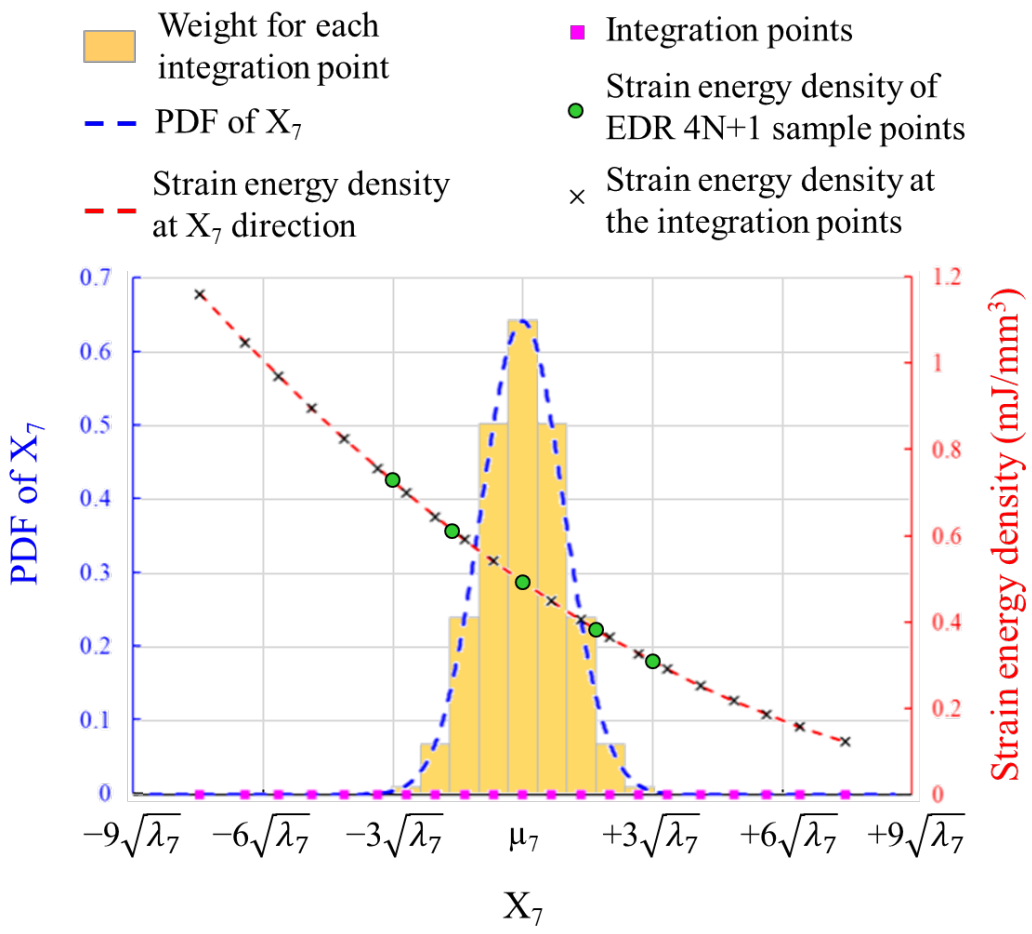

Figure 30 Integration points and weights for 1-D numerical integration for X_7 variable

Step 8

These statistical moments were then used to determine the measures of the PDF of system response, including the mean (μ), standard deviation (σ), skewness (β_1), and kurtosis (β_2), using Equations (5.18) to (5.21) [75]. The relationship between these four measures and a distribution was sketched in Figure 31.

$$\mu = E\{[Y(X_1, \cdots, X_N)]\} \tag{5.18}$$

$$\sigma = E\{[Y(X_1, \cdots, X_N) - E\{[Y(X_1, \cdots, X_N)]\}]^2\}^{1/2} \tag{5.19}$$

$$\beta_1 = \frac{E\{[Y(X_1, \cdots, X_N) - E\{[Y(X_1, \cdots, X_N)]\}]^3\}}{\sigma^3} \tag{5.20}$$

$$\beta_2 = \frac{E\{[Y(X_1, \cdots, X_N) - E\{[Y(X_1, \cdots, X_N)]\}]^4\}}{\sigma^4} \tag{5.21}$$

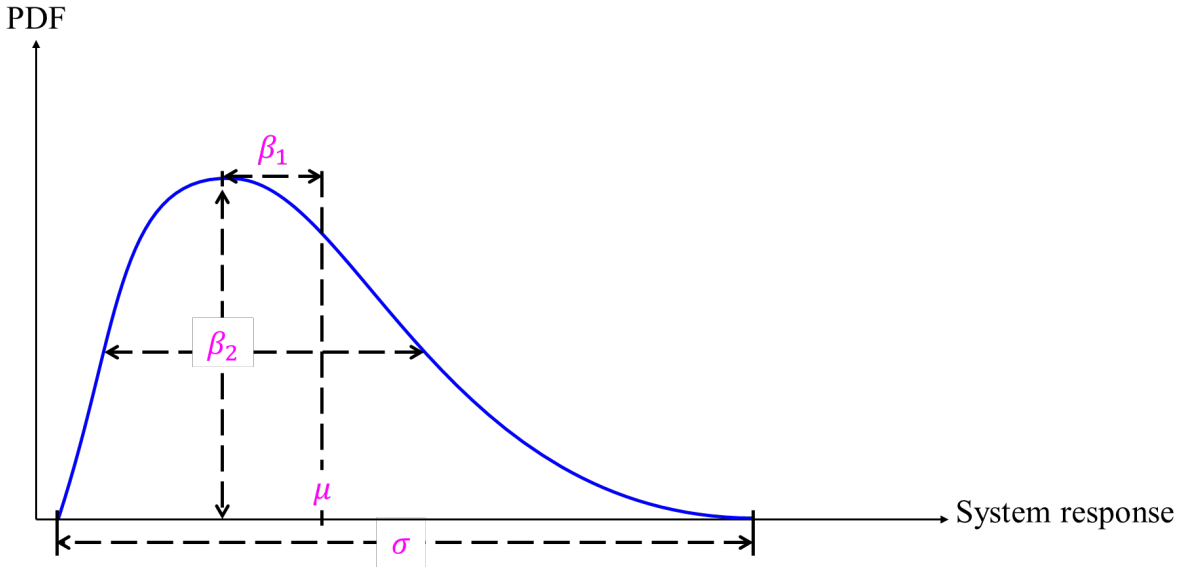

Figure 31 A sketch of the measures of a distribution

Step 9

We then calculated the following quantities (Equation 5.22) that are needed to specify the PDF of the system response using the Pearson system [76]:

$$
\begin{aligned}
c_0 &= (4\beta_2 - 3\beta_1^2)(10\beta_2 - 12\beta_1^2 - 18)^{-1}\sigma^2 \\
c_1 &= \beta_1(\beta_2 + 3)(10\beta_2 - 12\beta_1^2 - 18)^{-1}\sigma \\
c_2 &= (2\beta_2 - 3\beta_1^2 - 6)(10\beta_2 - 12\beta_1^2 - 18)^{-1} \\
a &= c_1
\end{aligned}
\tag{5.22}
$$

We then solved the differential equation (Equation 5.23) to determine the PDF of *Y*, the system response. There was no single solution for this differential equation because the solution, *p(Y)*, depended on the values of a, c_0, c_1, c_2, and the roots of $c_0 + c_1 Y + c_2 Y^2$.

$$
\frac{1}{p(Y)}\frac{dp(Y)}{dY} = -\frac{a + Y}{c_0 + c_1 Y + c_2 Y^2} \tag{5.23}
$$

For example, when c_1 = c_2 = 0, the Pearson distribution was Type 0, which was Normal distribution. The solution *p(Y)* was listed in Equation (5.24), where c_0 must be positive, and *K* = $\sqrt{2\pi c_0}$ to make $\int_{-\infty}^{+\infty} p(Y)dY = 1$.

$$
p(Y) = K \times exp\left[-\frac{(Y + a)^2}{2c_0}\right] \tag{5.24}
$$

On the other hand, when $c_1 \neq 0$, but $c_2 = 0$, the distribution was Pearson Type III, which was Gamma distribution. The solution *p(Y)* was listed in Equation (5.25), where $m = c_1^{-1}(c_0 c_1^{-1} - a)$, and *K* was the constant to make $\int_{-\infty}^{+\infty} p(Y)dY = 1$. If $c_1 > 0$, the range of Y was $Y > -c_0/c_1$. If $c_1 < 0$, the range of Y was $Y < -c_0/c_1$.

$$p(Y) = K \times (c_0 + c_1 x)^m \times exp\left[-\frac{x}{c_1}\right] \tag{5.25}$$

Note that the Pearson system assumes that the mean of the PDF equals 0, so we shifted the distribution to the mean μ after determining the solution *p(Y)*.

In order to tell the contribution of the input variable uncertainties on the final system response. Three different uncertainty scenarios were performed. The first scenario included the uncertainties of all input variables (X_1 to X_{11}). The second scenario considered the uncertainties related to solder joint (X_1 to X_5), and the third scenario incorporated the uncertainties that were not related to solder joint (X_6 to X_{11}). While performing the uncertainty scenario comparison, Step 2 to Step 9 were repeated for each scenario.

5.3 Results

The system responses at the 45 sample points are shown in Table 13. After obtaining these, we determined the statistical moments as well as the μ, σ, β_1, and β_2 using the equations described in Section 2. Among the eleven uncertain input variables, X_2, X_7 and X_{10} exhibited large contributions on the system response along their eigenvector directions.

Table 13 The system responses at the sample points. Note that all of the values for Y_{i3} are from the same sample point, where every variable equals its mean.

Variable i	Y_{i1}	Y_{i2}	Y_{i3}	Y_{i4}	Y_{i5}
X_1	0.4766	0.4757	0.4734	0.4717	0.4710
X_2	0.5556	0.5119	0.4734	0.4409	0.4128
X_3	0.4275	0.4503	0.4734	0.4979	0.5226
X_4	0.4724	0.4732	0.4734	0.4742	0.4750
X_5	0.4697	0.4717	0.4734	0.4757	0.4768
X_6	0.4600	0.4667	0.4734	0.4806	0.4869
X_7	0.6875	0.5758	0.4734	0.3830	0.3021
X_8	0.4257	0.4506	0.4734	0.4954	0.5153
X_9	0.4656	0.4696	0.4734	0.4778	0.4813
X_{10}	0.2982	0.3769	0.4734	0.5910	0.7282
X_{11}	0.4548	0.4647	0.4734	0.4817	0.4898

As shown in Table 14, the results of each uncertainty scenario yielded different distributions for the system response. The values of $(\beta_1)^2$, β_2, c_0, c_1, and c_2 were used to determine the type of distribution of the Pearson system. Johnson *et al.* [76] described the detailed criteria on categorizing the types of Pearson system.

Table 14 Summary of distribution characteristics with various uncertainty scenarios

Uncertainties	μ	σ	$(\beta_1)^2$	β_2	c_0	c_1	c_2	PDF type
All	0.4832	0.1010	0.0385	3.0606	0.0102	0.0099	0.0005	Type III
Exclude solder-related	0.4808	0.0978	0.0457	3.0689	0.0096	0.0104	0.0001	Type III
Exclude non-solder	0.4758	0.0254	0.0211	3.0372	0.0006	0.0008	0.0009	Type 0

Figure 32 shows the PDF of the system response for the three uncertainty scenarios. The uncertainties of the solder-related uncertain input variables made little contribution to the distribution of the overall system response. On the contrary, the uncertainties of the non-solder uncertain input variables, especially X_7 and X_{10} (CTE-related), took major contribution to the overall distribution of the system response. We were not surprised with the results because the CTE mismatch was considered as the major contributor of solder joint failure.

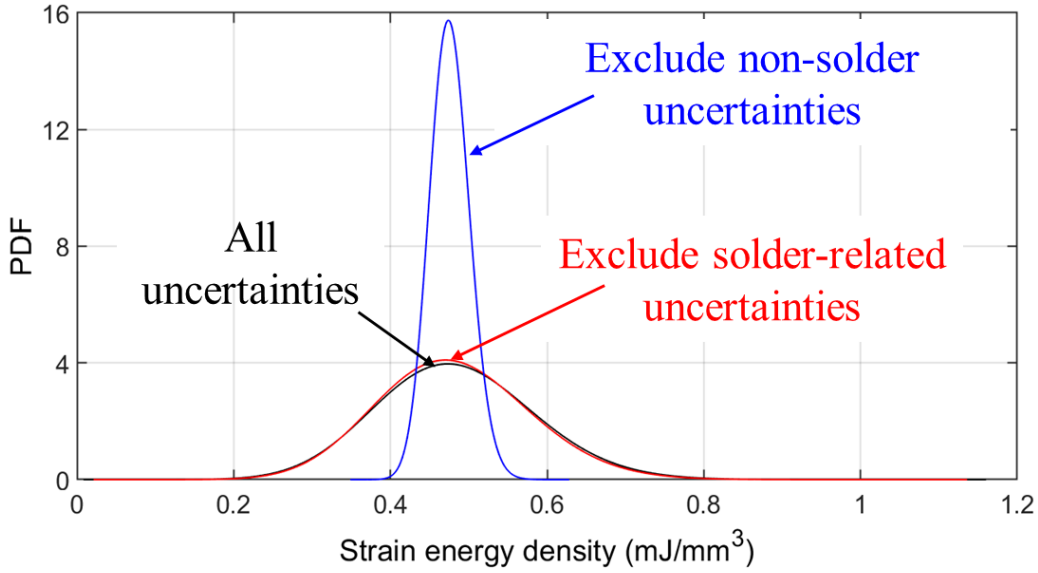

Figure 32 PDF comparison of system response with various uncertainty scenarios

In order to have a more consistent comparison of the system response and prepare for the CTF conversion, the cumulative distribution functions (CDFs) of the system responses were presented in Figure 33 by taking the integral of the PDF in Figure 32. The strain energy densities of CDF 10%, 50%, and 90% were calculate from comparison between the three uncertainty scenarios.

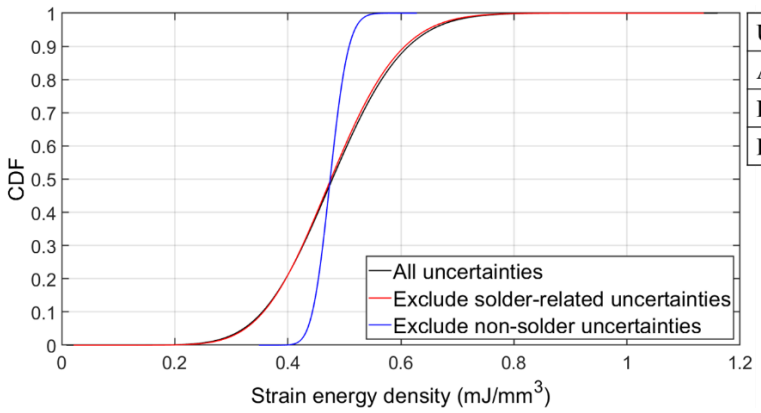

Uncertainties \ CDF	0.1	0.5	0.9
All	0.3548	0.4793	0.6140
Exclude solder-related	0.3560	0.4750	0.6062
Exclude non-solder	0.4434	0.4748	0.5086

Figure 33 CDF comparison of system response with various uncertainty scenarios

Finally, we converted the strain energy density to the cycles to failure (CTF) by applying different low-cycle energy-based fatigue models, as shown in Figure 34. For the CTF conversion, only the CDF of all uncertainties was performed because it contained the uncertainties of all the uncertain input variables. Three low-cycle energy-based fatigue models were selected for comparison, and their assumptions and constants of fatigue model were summarized in Table 15.

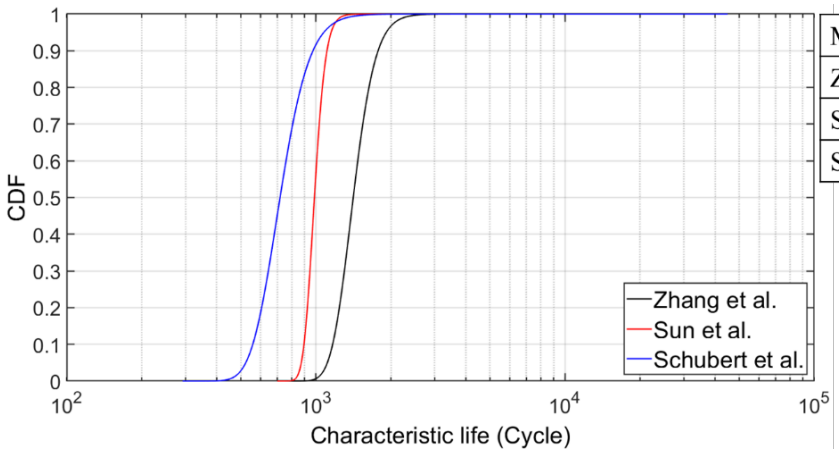

Model \ CDF	0.1	0.5	0.9
Zhang et al.	1169	1412	1776
Sun et al.	897	987	1110
Schubert et al.	559	720	976

Figure 34 CDF of the cycles to failure (characteristic life) with the conversion of various fatigue models

The difference between the CDFs of these three fatigue models were quantified by taking the CDF ratio at 0.1, 0.5, and 0.9. As shown in Figure 34, the cycle difference between Zhang *et al.* [11] and Schubert *et al.* [6] increased from 610 to 800 when the CDF ratio rose from 0.1 to 0.9. The differences between the fatigue models came from the model constants, which were decided by curve fitting with the field failure data and simulation strain energy density. The major factors that caused the simulated strain energy density variation between the three fatigue models were the type of strain energy density, the volume-weighted amount, and the cycle accumulation. The major difference from the field failure data was the life of prediction, including mean life (N50%) and characteristic life (N63.2%). The assumptions employed in Zhang *et al.*'s study [11] fitted the assumptions in this study most. Therefore, the characteristic life CDF of Zhang *et al.* [11] was used for the subsequent discussions.

Table 15 Assumptions and constants of three selected fatigue models

Prior studies	Strain energy density	Volume-weighted amount	Cycle accumulation	Fatigue coefficient	Fatigue exponent	Fatigue life prediction
Schubert *et al.* [6]	Viscoplastic	100%	Not specified	3.30×10^{-3}	−1.02	N63.2%
Sun *et al.* [10]	Creep	9.3%	Not specified	4.38×10^{-8}	−0.39	N63.2%
Zhang *et al.* [11]	Viscoplastic	5%	Cycle 3	1.69×10^{-4}	−0.77	N63.2%

5.4 Discussion

The distribution of cycles to failure can be modeled with a two-parameter Weibull CDF, as shown in Equation (5.26), where η is the scale parameter or characteristic life, and β is the shape parameter. Once the η and β are given, the CDF of the cycles to failure is determined. The CDF of characteristic life (presented in Section 4) is actually the distribution of η itself. By taking the CDF ratio of 0.1, 0.5, and 0.9, the variation of η can be defined, which are 1169, 1412, and 1776 cycles, respectively. Moreover, the failure mechanism of the BGA type component has been recognized as wear-out mechanism, which implies that $\beta > 1$. As shown in previous work, the variation of β is between 1 and 15 [6],[10],[11]. Therefore, β is chosen to be 1.5, 5, and 10 in this

study. The combinations of η and β values exhibit the distribution of the cycles to failure CDF of the solder joint between the BGA component and the PCB. Figure 35 to Figure 37 demonstrate the distributions.

$$F(t) = 1 - e^{-\left(\frac{t}{\eta}\right)^{\beta}} \tag{5.26}$$

For CDF ratio 0.1, the cycles increase when β rises from 1.5 to 10 no matter the η value is. This phenomenon indicates that higher failure rate situation (larger β) needs more cycles to cumulate 10% of failures, which is interesting because higher failure rate usually takes less cycles to achieve the same CDF ratio.

For CDF ratio 0.5, the cycles increment makes small effect (< 5%) after β is greater than 5, which means β doesn't play a key role while estimating the 50% failures of the solder joints. On the contrary, the η value makes larger differences on the cycles to failure when CDF ratio is 0.5, and the difference becomes larger when the β increases to 10.

For CDF ratio 0.9, the cycles to failure decreases when the β increases to 10 for all three η values. This fact meets with general agreement of the failure rate understanding. However, the decrement slowly decreases with the increasing β value, and the difference between $\beta = 5$ and $\beta = 10$ is less than 8%.

In the end, the tendency of cycles to failure changes depending on the CDF ratio. To have a reliable estimation on the cycles to failure, people need to know their goal, such as 10%, 50%, or 90% failures. According to the goal, the η and β values can play a different role. The evaluation

on the β value is also critical because the β value can make significant impact on the cycles to failure. For instance, the change of the cycles is the highest from $\beta = 1.5$ to $\beta = 5$ for all CDF ratios.

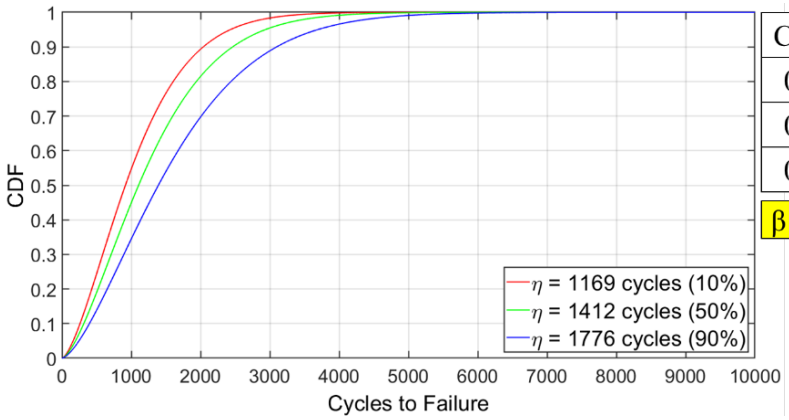

CDF	η = 1169	η = 1412	η = 1776
0.1	258	311	391
0.5	913	1102	1386
0.9	2027	2448	3080

β = 1.5

Figure 35 Cycles to failure CDF distributions ($\beta = 1.5$)

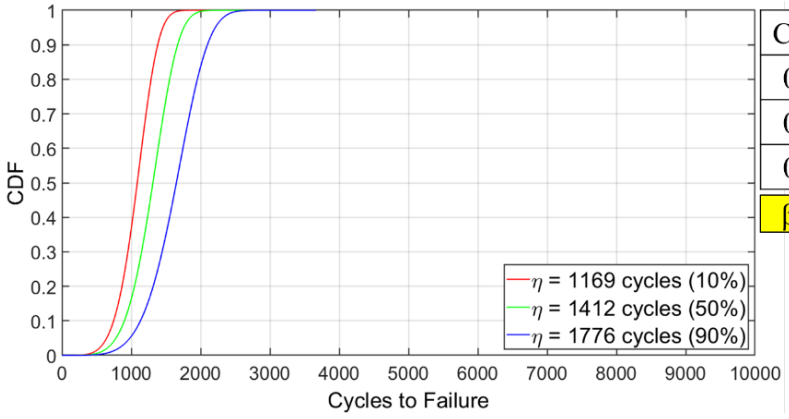

CDF	η = 1169	η = 1412	η = 1776
0.1	743	897	1128
0.5	1086	1311	1649
0.9	1379	1666	2095

β = 5

Figure 36 Cycles to failure CDF distributions ($\beta = 5$)

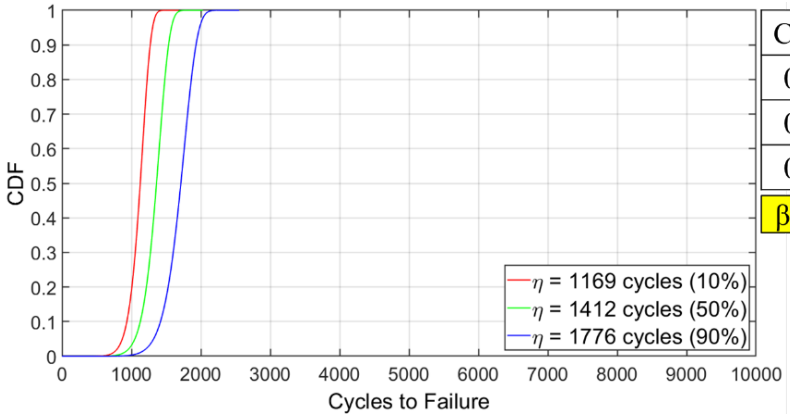

CDF	η = 1169	η = 1412	η = 1776
0.1	932	1126	1416
0.5	1127	1361	1712
0.9	1270	1534	1929

β = 10

Figure 37 Cycles to failure CDF distributions ($\beta = 10$)

To visualize the impact of the uncertainty on the distribution of the cycles to failure, four different uncertainty scenarios were selected, and the results are shown in Figure 38.

In Case A, the CDF 0.5 value of ΔW was used and converted to η with Chen *et al.*'s viscoplastic model [4]. The β value was chosen to be 1.5. In Case B, the CDF 0.1 and 0.9 values of ΔW were converted into η values. The fatigue model and β value remained the same as the values in Case A. In Case C, the β values were selected to be 1.5, 5, and 10. The others remained the same as the ones in Case B. The CDF curve with the same β value exhibited the same color. In Case D, the fatigue models were chosen to be the seven of nine published models. The other remained the same as the ones in Case C. The CDF curves from the same fatigue model showed the same color.

For each uncertainty scenario (Case A to Case D), the estimation on the mean life (N50%) or characteristic life (N63.2%) distribution is straightforward. The CDF ratio 0.5 and 0.632 indicate the mean life and characteristic life, respectively. For Case A, the estimation is a single value. For Case B, the estimation is the interval between the two lines. For Case C, the estimations include three separate intervals from the three pairs of lines. For Case D, the estimations will combine 21 separate intervals from all the 21 pairs of lines (three different β values multiplied by seven low-cycle energy-based fatigue models).

Case A: One ΔW value, one fatigue model, and one value of β

Case B: Distribution of ΔW, one fatigue model, and one value of β

Case C: Distribution of ΔW, one fatigue model, and range of β

Case D: Distribution of ΔW, multiple fatigue models, and range of β

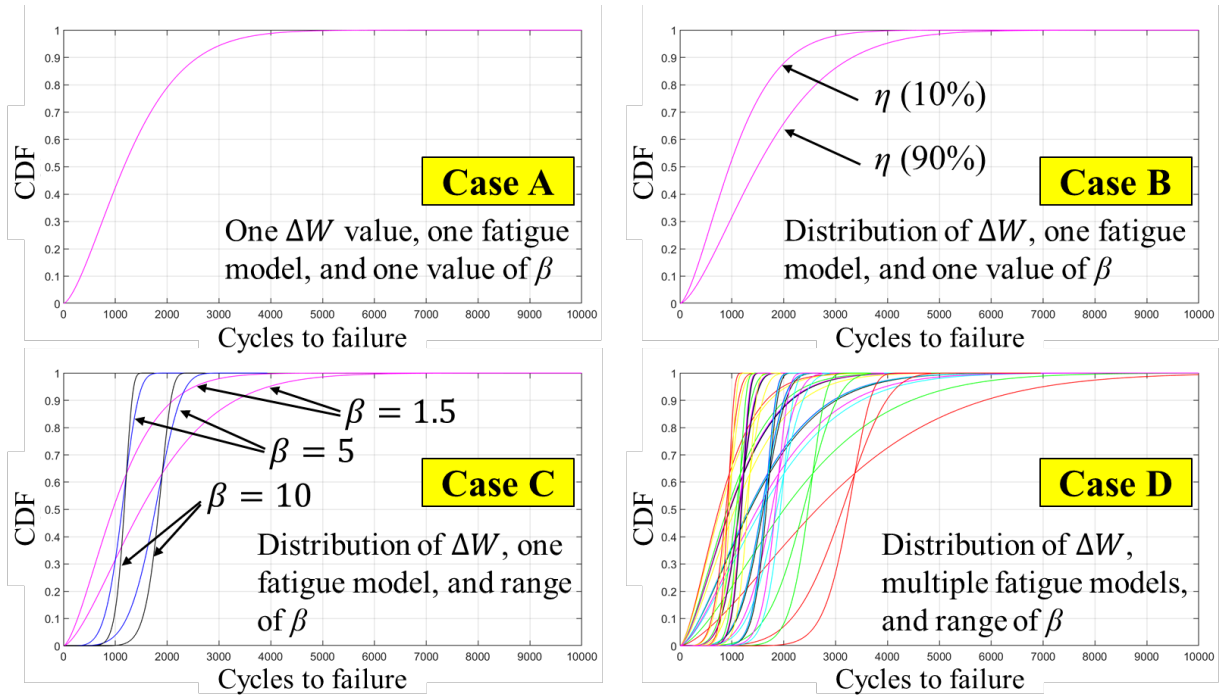

Figure 38 Case studies for various uncertainty scenarios. Case A: One ΔW value, one fatigue model, and one value of β. Case B: Distribution of ΔW, one fatigue model, and one value of β. Case C: Distribution of ΔW, one fatigue model, and range of β. The colors mean different β values. Case D: Distribution of ΔW, multiple fatigue model, and range of β. The colors mean different fatigue models.

5.5 Summary

This chapter demonstrated the interval estimation of the cycles to failure distribution of solder joints between the ball grid array (BGA) component and printed circuit board (PCB) by using the eigenvector dimension reduction (EDR) method and FEA simulation tool. The eleven uncertain input variables were first determined via basic mechanics theory, and then the distribution of the

strain energy density accumulation was determined as the system response by employing the EDR method. Due to the consideration of fatigue life prediction, we selected specific fatigue models, which predicted characteristic life (N63.2%) of the cycles to failure, to convert the strain energy density to cycles to failure and obtained the distribution of the characteristic life. The cumulative distribution function (CDF) ratio of 0.1, 0.5, and 0.9 were used to get the interval of characteristic life, which was the scale parameter η for a two-parameter Weibull distribution. Combining with different scenarios of β values, the distributions of the cycles to failure CDFs were presented in the end.

From the uncertainty propagation perspective, the uncertainties related to solder joint (X_1 to X_5) made little contribution to the uncertainty of system response. On the contrary, the uncertainties that not related to solder joint (X_6 to X_{11}) had significant effect on the overall uncertainty. This suggests that the coefficient of thermal expansion (CTE) mismatch was a critical factor for BGA assembly failures. While converting to cycles, different fatigue models exhibited different CDFs for the cycles to failure. Therefore, understanding the underlying assumptions of the fatigue model was supreme before using them. We suggested choosing the fatigue model with closet assumptions to your own study.

For predicting the distribution of the fatigue life of the solder joint, we obtained the interval of characteristic life from the distribution of the system response, which was converted to cycles to failure as well. Combining the selected shape parameter values, the CDF distributions of the fatigue life of solder joint were determined. For different CDF ratios, the cumulated failures were affected by the shape parameter in different ways. For example, for CDF ratio 0.1, the cycles to failure showed the same trend with the shape parameter, whereas for CDF ratio 0.9, the trend was

opposite. Hence, knowing the information of the shape parameter can help to narrow down the estimation interval of the fatigue life.

Knowing which variables contribute the most to the uncertainty about the characteristic life can guide efforts to reduce this uncertainty. In particular, the firm should emphasize reducing the variability of the input variables that have the most impact. Characterizing the uncertainty about the characteristic life can also guide solder material selection decisions.

Chapter 6: Contributions and Future Work

This chapter is organized as follows. In Section 6.1, we provide the conclusions of this dissertation. The contributions of this dissertation are demonstrated in Section 6.2. Future work is pointed out in Section 6.3.

6.1 Overview

To answer the first research question, we compared and summarized nine published low-cycle energy-based fatigue models for the durability of solder joint. We found that the divergence of these low-cycle fatigue models came from the last step of FEA simulation, which was the step of determining strain energy density. This step can be affected by strain energy density type, volume-weighted amount, and cycle accumulation, which are different among the low-cycle fatigue model studies.

To answer the second research question, adjustment is necessary before comparing the low-cycle fatigue models. After adjusting the inconsistency of the strain energy density methods, seven of the nine low-cycle fatigue models exhibited excellent consistency around 1 mJ/mm^3 strain energy density, and it's suitable for various solder materials and components. The remaining two low-cycle fatigue models still showed large divergence after the adjustment because of three major factors. Frist, these two models only had three data points, which were lager than1 mJ/mm^3 and some of them were larger than 5 mJ/mm^3. Second, their strain energy density range was smaller than the range of the values in the other studies. Third, these two deviated fatigue models did not apply volume-weighted averaging technique for calculating the strain energy density, but used the

maximum value from a single element. These three factors caused large deviation while curve fitting, and it cannot be improved by our adjustment methods.

To answer the third research question, we applied eigenvector dimension reduction (EDR) method for uncertainty propagation analysis for the ball grid array (BGA) component and printed circuit board (PCB) application. The EDR method significantly reduced the amount of FEA simulation while considering 11 uncertain input variables, and exhibited the uncertainty of the system response, which was the strain energy density accumulation. The contribution of the uncertain input variables on the system response was also studied, and we found the input variables that not related to solder joint made significant impact. These input variables were related to the component and the printed circuit board, especially for the coefficient of thermal expansion.

To answer the fourth research question, we compared the FEA simulation runs among the EDR method and response surface method (RSM), and Monte Carlo simulation. The EDR method showed excellent efficiency on performing the uncertainty propagation for the solder joint under temperature cycling. We obtained the distribution of the characteristic life (N63.2%) by putting the strain energy density value in the selected fatigue model. In the end, the distribution of cumulative distribution function (CDF) of the cycles to failure of the studied solder joint can be determined by incorporating various uncertainty sources.

6.2 Contributions

We developed an innovative approach for clustering and comparing the consistency of the published low-cycle energy-based fatigue models with meta-analysis techniques and FEA simulation. First, the results pointed out these low-cycle energy-based fatigue models were suitable for predicting the fatigue life of a solder joint with various lead-free solder materials, components, and PCBs. Second, we believe the acceptable divergence among the seven of nine models was caused during the curve fitting procedure between the field data and simulation results in each study. The adjusted results from the other two models were not consistent with the results from the other models, however, due to their studied strain energy density range, the number of data points for curve fitting, and not using the volume-weighted averaging technique for strain energy density calculation. These results and findings can be treated as the precaution while employing the selected fatigue models or building a new low-cycle energy-based fatigue model for the engineers. Third, this approach created a new technique for the engineers to evaluate other type of fatigue model from many of the published studies. The evaluation process should be quite similar.

We created a new uncertainty propagation approach that included meta-analysis techniques, prior information collection, strain energy density adjustment, mean life/characteristic life conversion, and EDR method. First, this new uncertainty propagation approach can distinguish a variety of uncertain factors, such as geometry, material property, constitutive law, simulation method, and fatigue model. The uncertain factors can be quantified as separate distributions and are affected by prior information and simulation results. Second, the uncertainties came from the component and PCB dominated the final system uncertainty while evaluating the solder joint durability under temperature cycling. This finding actually lessens the importance of the prior

information of solder materials. Third, our new approach saves sufficient computational costs by only running 4N+1 or 2N+1 (if the response is most linear) FEA simulations, where N is the number of uncertain input variables. The engineers can then estimate the uncertainty of the solder joint durability efficiently.

6.3 Future Work

One possible future direction is to explore the external validity of our method for various components with temperature cycling situations. Some of the published studies actually provide the information of cycles to failure (data points in Weibull plot) for specific components (strain energy density value). By utilizing the methods in this dissertation, the distribution of the CDF of solder joint failure can be estimated and then compared to the field data points. The experiments can be conducted with various values of the shape parameter to observe the relationships between our predicted CDF distribution and the field data points.

Another possible future work is to apply the methodology in this dissertation for other type of fatigue model (i.e. crack growth) or other failure mechanisms, such as high-cycle fatigue. By doing the first one, we can conduct the cross comparison between different types of fatigue models. There are many published studies (separate yet related) on different failure mechanisms of the solder joint. While conducting the second one, we expect to generate new and interesting findings for these specific failure mechanisms as well.

Bibliography

[1] Cheng, S., Huang, C.M. and Pecht, M., 2017. A Review of Lead-Free Solders for Electronics Applications. *Microelectronics Reliability*, 75, pp.77-95.

[2] Huang, C.M., Romero, J.A., Osterman, M., Das, D. and Pecht, M., 2019. Life Cycle Trends of Electronic Materials, Processes and Components. *Microelectronics Reliability*, 99, pp.262-276.

[3] Lau, J.H. and Pao, Y.H., 1997. Solder Joint Reliability of BGA, CSP, Flip Chip, and Fine Pitch SMT Assemblies. McGraw-Hill Professional Publishing.

[4] Chen, D.Y., Osterman, M. and Dasgupta, A., 2020. Energy Based Modeling for Temperature Cycling Induced Tin Silver Copper Solder Interconnect Fatigue Life. *Microelectronics Reliability*, 109, p.113651.

[5] Syed, A., 2004, June. Accumulated Creep Strain and Energy Density Based Thermal Fatigue Life Prediction Models for SnAgCu Solder Joints. In *2004 Proceedings. 54th electronic components and technology conference (IEEE Cat. No. 04CH37546)* (Vol. 1, pp. 737-746). IEEE.

[6] Schubert, A., Dudek, R., Auerswald, E., Gollhardt, A., Michel, B. and Reichl, H., 2003, May. Fatigue Life Models for SnAgCu and SnPb Solder Joints Evaluated by Experiments and Simulation. In *Electronic components and technology conference* (pp. 603-610). IEEE; 1999.

[7] Hsieh, M.C., 2015, October. Modeling Correlation for Solder Joint Fatigue Life Estimation in Wafer-Level Chip Scale Packages. In *2015 10th International Microsystems, Packaging, Assembly and Circuits Technology Conference (IMPACT)* (pp. 65-68). IEEE.

[8] Hsieh, M.C. and Tzeng, S.L., 2014, August. Solder Joint Fatigue Life Prediction in Large Size and Low Cost Wafer-Level Chip Scale Packages. In *2014 15th International Conference on Electronic Packaging Technology* (pp. 496-501). IEEE.

[9] Ghorbani, H.R. and Spelt, J.K., 2007. An Analytical Elasto-Creep Model of Solder Joints in Leadless Chip Resistors: Part 2—Applications in Fatigue Reliability Predictions for SnPb and Lead-Free Solders. *IEEE Transactions on Advanced Packaging*, 30(4), pp.695-704.

[10] Sun, W., Zhu, W.H., Danny, R., Che, F.X., Wang, C.K., Sun, A.Y. and Tan, H.B., 2007, April. Study on the Board-Level SMT Assembly and Solder Joint Reliability of Different QFN Packages. In *2007 International Conference on Thermal, Mechanical and Multi-Physics Simulation Experiments in Microelectronics and Micro-Systems. EuroSime 2007* (pp. 1-6). IEEE.

[11] Zhang, Q., Dasgupta, A., Nelson, D., and Pallavicini, H. (January 6, 2005). Systematic Study on Thermo-Mechanical Durability of Pb-Free Assemblies: Experiments and FE Analysis. *ASME. Journal of Electronic Packaging*, December 2005; 127(4): 415–429.

[12] Matt, G.E., Brewer, A. and Sklar, M., 2010. External Validity. *Quantitative Methods and Research Design*, pp.521-527.

[13] Mikolajewicz, N. and Komarova, S.V., 2019. Meta-Analytic Methodology for Basic Research: a Practical Guide. *Frontiers in physiology*, 10, p.203.

[14] Wei, H.P., 2018. *Advanced Statistical Analysis for Tail-End Probability Prediction and Performance Response Calculation of Semiconductor Packaging Products with a Large Number of Input Variables* (Doctoral dissertation, University of Maryland, College Park).

[15] Borgesen, P., Wentlent, L., Khasawneh, S., Shirazi, S., Schmitz, D., Alghoul, T., Greene, C. and Yin, L., 2018. A Mechanistic Thermal Fatigue Model for SnAgCu Solder Joints. *Journal of Electronic Materials*, 47(5), pp.2526-2544.

[16] Green, W.B., 1961. A Fatigue-Free Silicon Device Structure. *Transactions of the American Institute of Electrical Engineers, Part I: Communication and Electronics*, 80(2), pp.186-192.

[17] Akay, H.U., Paydar, N.H. and Bilgic, A., 1997. Fatigue Life Predictions for Thermally Loaded Solder Joints using a Volume-Weighted Averaging Technique. *Journal of Electronic Packaging*, 119(4), pp. 228-235.

[18] Lee, W.W., Nguyen, L.T. and Selvaduray, G.S., 2000. Solder Joint Fatigue Models: Review and Applicability to Chip Scale Packages. *Microelectronics reliability*, 40(2), pp.231-244.

[19] Su, S., Akkara, F.J., Thaper, R., Alkhazali, A., Hamasha, M. and Hamasha, S.D., 2019. A State-of-the-Art Review of Fatigue Life Prediction Models for Solder Joint. *Journal of Electronic Packaging*, 141(4), p.040802.

[20] Morrow, J., 1965. Cyclic Plastic Strain Energy and Fatigue of Metals. In *Internal friction, damping, and cyclic plasticity. ASTM International*. Lazan, B.J. (edited). West Conshohocken, PA, USA.

[21] Dasgupta, A., Oyan, C., Barker, D., and Pecht, M. (June 1, 1992). Solder Creep-Fatigue Analysis by an Energy-Partitioning Approach. ASME. *Journal of Electronic Packaging*, June 1992; 114(2): 152–160.

[22] Solomon, H. D., and Tolksdorf, E. D. (June 1, 1995). Energy Approach to the Fatigue of 60/40 Solder: Part I—Influence of Temperature and Cycle Frequency. ASME. *Journal of Electronic Packaging*, June 1995; 117(2): 130–135.

[23] Shi, X.Q., Pang, H.L.J., Zhou, W. and Wang, Z.P., 1999. A Modified Energy-Based Low Cycle Fatigue Model for Eutectic Solder Alloy. *Scripta Materialia*, 41(3), pp.289-296.

[24] Syed, A., 2001, May. Predicting Solder Joint Reliability for Thermal, Power, and Bend Cycle within 25% Accuracy. In 2001 *Proceedings. 51st Electronic Components and Technology Conference (Cat. No. 01CH37220)* (pp. 255-263). IEEE.

[25] Monkman, F.C., 1956. An Empirical Relationship between Rupture Life and Minimum Creep Rate in Creep Rupture Tests. In *proceeding of ASTM* (Vol. 56, pp. 91-103).

[26] Miner, M. A. (March 9, 2021). Cumulative Damage in Fatigue. ASME. *Journal of Applied Mechanics*, September 1945; 12(3): A159–A164.

[27] JESD22-A104F, Temperature cycling, JEDEC Standard, 2020.

[28] Mawer, A., Vo, N., Johnson, Z. and Lindsay, W., 1999, June. Board-Level Characterization of 1.0 and 1.27 mm Pitch PBGA for Automotive Under-Hood Applications. In *1999 Proceedings. 49th Electronic Components and Technology Conference (Cat. No. 99CH36299)* (pp. 118-124). IEEE.

[29] Callister, W.D. and Rethwisch, D.G., 2018. Materials Science and Engineering: An introduction (10^{th} edition), (Vol. 7, pp. 665-715). New York: *John Wiley & sons.*, Chapter 7. ISBN number: 9781119405498.

[30] Garofalo, F., 1965. Fundamentals of Creep and Creep-Rupture in Metals. *Macmillan series in materials science*. New York, Macmillan Co., London, Collier-Macmillan, LTD., 1965. 258 Pages.

[31] Anand, L., 1982. Constitutive Equations for the Rate-Dependent Deformation of Metals at Elevated Temperatures, *Journal of Engineering Material Technology*, January 1982, 104(1): 12-17.

[32] Basit, M., Ahmed, S., Motalab, M., Roberts, J.C., Suhling, J.C. and Lall, P., 2016, May. The Anand Parameters for SAC Solders after Extreme Aging. In *2016 15th IEEE Intersociety Conference on Thermal and Thermomechanical Phenomena in Electronic Systems (ITherm)* (pp. 440-447). IEEE.

[33] Hassan, K.R., Alam, M.S., Wu, J., Suhling, J.C. and Lall, P., 2020, July. Isothermal Aging Dependent Anand Parameters of SAC305 Lead Free Solder at Extreme High Temperatures. In *2020 19th IEEE Intersociety Conference on Thermal and Thermomechanical Phenomena in Electronic Systems (ITherm)* (pp. 1191-1200). IEEE.

[34] Herkommer, D., Punch, J. and Reid, M., 2012. Constitutive Modeling of Joint-Scale SAC305 Solder Shear Samples. *IEEE Transactions on Components, Packaging and Manufacturing Technology*, 3(2), pp.275-281.

[35] Bai, N., Chen, X. and Gao, H., 2009. Simulation of Uniaxial Tensile Properties for Lead-Free Solders with Modified Anand Model. *Materials & Design*, 30(1), pp.122-128.

[36] Haq, M.A., Hoque, M.A., Suhling, J.C. and Lall, P., 2020, October. Determination of Anand Parameters from Creep Testing of SAC305 Solder Joints. In *International Electronic Packaging Technical Conference and Exhibition* (Vol. 84041, p. V001T01A016). American Society of Mechanical Engineers.

[37] Motalab, M., Basit, M., Suhling, J.C., Bozack, M.J. and Lall, P., 2014, May. Creep Test Method for Determination of Anand Parameters for Lead Free Solders and Their Variation with Aging. In *Fourteenth Intersociety Conference on Thermal and Thermomechanical Phenomena in Electronic Systems (ITherm)* (pp. 127-141). IEEE.

[38] Libot, J.B., Dulondel, F., Milesi, P., Alexis, J., Arnaud, L. and Dalverny, O., 2018, May. Experimental Strain Energy Density Dissipated in SAC305 Solder Joints during Different Thermal Cycling Conditions Using Strain Gages Measurements. In *2018 IEEE 68th Electronic Components and Technology Conference (ECTC)* (pp. 748-755). IEEE.

[39] Mysore, K., Subbarayan, G., Gupta, V. and Zhang, R., 2009. Constitutive and Aging Behavior of Sn3. 0Ag0. 5Cu Solder Alloy. *IEEE Transactions on Electronics Packaging Manufacturing*, 32(4), pp.221-232.

[40] Chang, J., Wang, L., Dirk, J. and Xie, X., 2006. Finite Element Modeling Predicts the Effects of Voids on Thermal Shock Reliability and Thermal Resistance of Power Device. *Welding journal*, 85(3), pp.63s-70s.

[41] Janz, D.T., 2004. Reliability of Discrete Power Devices with Lead Free Solder Joints. *Master's Thesis*, Institute for Microsystem Technology, Albert Ludwigs.

[42] Lee, H., Liu, R., Park, S. and Kwak, J., 2014, November. Characterization of Creep Behavior of Actual Lead-Free Solder Joint for Modeling. In *ASME International Mechanical Engineering Congress and Exposition* (Vol. 46590, p. V010T13A071). American Society of Mechanical Engineers.

[43] Vianco, P.T., 2005. Fatigue and Creep of Lead-Free Solder Alloys: Fundamental Properties. *ASM International*, 67, Chapter 3.

[44] Clech, J.P., 2007. Chapter 2: Review and Analysis of Lead-Free Solder Material Properties. Lead-Free Electronics: iNEMI Projects Lead to Successful Manufacturing. Editors: Bradley, E., Handwerker C. A., Bath J., Parker R. D., Gedney R. W. *A John Wiley&Sons, Inc.*, Publication.

[45] Cuddalorepatta, G. and Dasgupta, A., 2008, April. Effect of Primary Creep Behavior on Fatigue Damage Accumulation Rates in Accelerated Thermal Cycling of Sn3. 0Ag0. 5Cu Pb-free Interconnects. In *EuroSimE 2008-International Conference on Thermal, Mechanical and Multi-Physics Simulation and Experiments in Microelectronics and Micro-Systems* (pp. 1-8). IEEE.

[46] Darveaux, R. and Reichman, C., 2007, May. Mechanical Properties of Lead-Free Solders. In *2007 Proceedings 57th Electronic Components and Technology Conference* (pp. 695-706). IEEE.

[47] Le, W.K., Zhou, J.Y., Ke, C.B., Zhou, M.B. and Zhang, X.P., 2020. Study of Accelerated Shear Creep Behavior and Fracture Process of Micro-Scale Ball Grid Array (BGA) Structure Cu/Sn–3.0 Ag–0.5 Cu/Cu Joints under Coupled Electro-Thermo-Mechanical Loads. *Journal of Materials Science: Materials in Electronics*, 31(18), pp.15575-15588.

[48] Jiang, Q., Deshpande, A. and Dasgupta, A., 2022. Multi-Scale Crystal Viscoplasticity Approach for Estimating Anisotropic Steady-State Creep Properties of Single-Crystal SnAgCu Alloys. *International Journal of Plasticity*, 153, p.103271.

[49] Paydar, N., Tong, Y. and Akay, H.U., 1994. A Finite Element Study of Factors Affecting Fatigue Life of Solder Joints. *Journal of Electronic Packaging*, Dec 1994, 116(4): 265-273.

[50] Bilgic, A., 1996, Fatigue Life Prediction Methods for Thermally Loaded Solder Joints Using the Finite Element Method, *M.S. thesis*, Purdue University, Indianapolis, IN.

[51] Wei, H.P., Han, B., Youn, B.D., Shin, H., Kim, I. and Moon, H., 2017. Assembly Yield Prediction of Plastically Encapsulated Packages with a Large Number of Manufacturing Variables by Advanced Approximate Integration Method. *Microelectronics Reliability*, 78, pp.319-330.

[52] Wei, H.P., Yang, Y.H., Wu, B. and Han, B., 2018, May. Prediction of Statistical Distribution of Vibration-Induced Solder Fatigue Failure Considering Intrinsic Variations of Mechanical Properties of Anisotropic Sn-Rich Solder Alloys. In *2018 IEEE 68th Electronic Components and Technology Conference (ECTC)* (pp. 741-747). IEEE.

[53] Thakur, Y.S. and Sakravdia, D.K., 2018. Reliability Prediction Methods for Electronic Devices and Systems-A Review. *International journal of applied engineering research*, vol, 13, pp.13063-13069.

[54] Darbandi, P., Bieler, T.R., Pourboghrat, F. and Lee, T.K., 2014. The Effect of Cooling Rate on Grain Orientation and Misorientation Microstructure of SAC105 Solder Joints before and after Impact Drop Tests. *Journal of electronic materials*, 43(7), pp.2521-2529.

[55] Kim, Y.K. and Hwang, D.S., 2015. PBGA Packaging Reliability Assessments under Random Vibrations for Space Applications. *Microelectronics Reliability*, 55(1), pp.172-179.

[56] Zuo, Y., Ma, L., Guo, F., Qiao, L., Shu, Y., Lee, A. and Subramanian, K.N., 2014. Effects of Electromigration on the Creep and Thermal Fatigue Behavior of Sn58Bi Solder Joints. *Journal of electronic materials*, 43(12), pp.4395-4405.

[57] Song, F., Lo, J.C., Lam, J.K., Jiang, T. and Lee, S.R., 2008, May. A Comprehensive Parallel Study on the Board Level Reliability of SAC, SACX and SCN Solders. In *2008 58th Electronic Components and Technology Conference* (pp. 146-154). IEEE.

[58] Jayaram, V., McCann, S., Singh, B., Pulugurtha, R., Smet, V., Tummala, R., Matsuura, H. and Takagi, Y., 2017, May. Analysis of System-Level Reliability of Single-Chip Glass BGA Packages with Advanced Solders and Polymer Collars. In *2017 IEEE 67th Electronic Components and Technology Conference (ECTC)* (pp. 1405-1412). IEEE.

[59] Singh, B., Huang, T.C., Kawamoto, S., Sundaram, V., Pulugurtha, R., Smet, V. and Tummala, R., 2016, May. Demonstration of Enhanced System-Level Reliability of Ultra-Thin BGA Packages with Circumferential Polymer Collars and Doped Solder Alloys. In *2016 IEEE 66th Electronic Components and Technology Conference (ECTC)* (pp. 1377-1385). IEEE.

[60] Singh, B., Menezes, G., McCann, S., Jayaram, V., Ray, U., Sundaram, V., Pulugurtha, R., Smet, V. and Tummala, R., 2017. Board-Level Thermal Cycling and Drop-Test Reliability of Large, Ultrathin Glass BGA Packages for Smart Mobile Applications. *IEEE Transactions on Components, Packaging and Manufacturing Technology*, 7(5), pp.726-733.

[61] Osterman, M., 2018, September. Modeling Temperature Cycle Fatigue Life of Select SAC Solders. In *Proceedings of SMTA International*. Online available: https://web.calce.umd.edu/lead-free/SMTAI2018-Osterman.pdf

[62] Xie, W., Liu, K.C. and Brillhart, M., 2009, January. Pb-Free Thin Small Outline Package (TSOP) Board Level Reliability Study. In *International Electronic Packaging Technical Conference and Exhibition* (Vol. 43598, pp. 775-780).

[63] Arnold, J., Blattau, N., Hillman, C., Solutions, D. and Sweatman, K., 2008. Reliability Testing of Ni-Modified SnCu and SAC305, *Accelerated Thermal Cycling. Resistor*, 1(1), p.1.

[64] Coyle, R., Johnson, C., Hillman, D., Pearson, T., Osterman, M., Smetana, J., Howell, K., Zhang, H., Silk, J., Geng, J. and Daily, D., Enhancing Thermal Fatigue Reliability of Pb-Free Solder Alloys with Additions of Bismuth and Antimony. *Proceedings of SMTA International*, Sep. 28 - Oct. 23, 2020. pp. 339-354.

[65] Tee, T.Y., Ng, H.S., Yap, D., Baraton, X. and Zhong, Z., 2003. Board Level Solder Joint Reliability Modeling and Testing of TFBGA Packages for Telecommunication Applications. *Microelectronics Reliability*, 43(7), pp.1117-1123.

[66] Schubert, A., Dudek, R., Walter, H., Jung, E., Gollhardt, A., Michel, B. and Reichl, H., 2002, May. Reliability Assessment of Flip-Chip Assemblies with Lead-Free Solder Joints. In *52nd Electronic Components and Technology Conference 2002. (Cat. No. 02CH37345)* (pp. 1246-1255). IEEE.

[67] Zhuang, W.D., Chang, P.C., Chou, F.Y. and Shiue, R.K., 2001. Effect of Solder Creep on the Reliability of Large Area Die Attachment. *Microelectronics Reliability*, 41(12), pp.2011-2021.

[68] Tee, T.Y., Ng, H.S. and Zhong, Z., 2006. Board Level Solder Joint Reliability Analysis of Stacked Die Mixed Flip-Chip and Wirebond BGA. *Microelectronics Reliability*, 46(12), pp.2131-2138.

[69] IPC-2581 B Test Case 3, IPC-DPMX (IPC-2581) Consortium. Online available: http://www.ipc2581.com/b-test-cases/

[70] Qian, C., Gheitaghy, A.M., Fan, J., Tang, H., Sun, B., Ye, H. and Zhang, G., 2018. Thermal Management on IGBT Power Electronic Devices and Modules. *IEEE Access*, 6, pp.12868-12884.

[71] Calabretta, M., Sitta, A., Oliveri, S.M. and Sequenzia, G., 2021. Power Semiconductor Devices and Packages: Solder Mechanical Characterization and Lifetime Prediction. *IEEE Access*, 9, pp.22859-22867.

[72] Youn, B.D., Xi, Z. and Wang, P., 2008. Eigenvector Dimension Reduction (EDR) Method for Sensitivity-Free Probability Analysis. *Structural and Multidisciplinary Optimization*, 37, pp.13-28.

[73] SAC305 | Pb-free Solder Spheres, CAPLINQ Corporation © 2023. Online available: https://www.caplinq.com/sac305-leadfree-solder-spheres-and-solder-balls.-low-cost-with-excellent-fatigue-resistance.-sac305.html#:~:text=Melting%20Temperature%20(Liquidus)%3A%20219,Spheroid%20Tolerance%20%3A%20Within%201.5%25

[74] Rahman, S. and Xu, H., 2004. A Univariate Dimension-Reduction Method for Multi-Dimensional Integration in Stochastic Mechanics. *Probabilistic Engineering Mechanics*, 19(4), pp.393-408.

[75] Kenett, R. and Zacks, S., 1998. Modern Industrial Statistics: Design and Control of Quality and Reliability: *Brooks*.

[76] Johnson, N.L., Kotz, S. and Balakrishnan, N., 1994. Continuous Univariate Distributions, Volume 1 (Vol. 163). *John Wiley & Sons*.